

The Turbulent Dynamics of Anticyclonic Submesoscale Headland Wakes[©]

TOMAS CHOR^{IP,a} AND JACOB O. WENEGRAT^a

^a Department of Atmospheric and Oceanic Science, University of Maryland, College Park, College Park, Maryland

(Manuscript received 22 August 2024, in final form 4 December 2024, accepted 10 March 2025)

ABSTRACT: Flow interacting with bathymetry has been posited to be important for dissipation and mixing in the global ocean. Despite this, there are large uncertainties regarding mixing in these environments, particularly as it pertains to the role of submesoscale structures in the dynamics and energetics. In this work, we study such flows with a series of large-eddy simulations of a submesoscale flow past a headland where the turbulence is resolved, allowing us to probe into the small-scale processes responsible for the energy cascade. One key finding is that the kinetic energy (KE) dissipation rate, buoyancy mixing rate, and eddy diffusivity of the flow organize as linear functions of the bulk Rossby and Froude numbers across all simulations, despite very different dynamical regimes. The slope Burger number (Rossby over Froude number) was found to be particularly useful as it can organize aspects of both the dynamics and energetics. Moreover, comparison of KE dissipation rates with previous works suggests an underestimation of dissipation rates by regional models of up to an order of magnitude, with potential implications for global energy budgets. Consistent with hypotheses from previous studies, but resolved here for the first time up to small scales, we find evidence of submesoscale centrifugal-symmetric instabilities (CSIs) in the wake leading to a forward energy cascade. However, given that dissipation and mixing rates seem to follow the same scaling across regimes with and without CSIs, their effect on flow energetics here differs from what has been observed in the upper ocean, where CSI turbulence seems to follow a different scaling from their non-CSI counterparts.

KEYWORDS: Ocean; Bottom currents; Dynamics; Small scale processes; Turbulence

1. Introduction

Coastal bathymetric features shape nearshore ocean circulations and directly impact physical and biological processes unique to these areas, such as dispersion of nutrients, dissolved pollutants, floating organisms, and sediment (St John and Pond 1992; Wang et al. 1999; Bastos et al. 2003; Nencioli et al. 2011; Ben Hamza et al. 2015). Importantly, for the present study, as sites of flow–bathymetry interactions, they also tend to be locations of intensive turbulence generation (Jalali and Sarkar 2017; Johnston et al. 2019; Capó et al. 2023; Radko 2023; Mashayek 2023; Whitley and Wenegrat 2025), leading to elevated rates of kinetic energy (KE) dissipation and buoyancy mixing (Munk and Wunsch 1998; Nikurashin and Ferrari 2011; Melet et al. 2013; McDougall and Ferrari 2017; Polzin and McDougall 2022). This mixing can be generated through a variety of dynamical processes (reviewed further below) and has been shown to impact large-scale budgets (Polzin et al. 1997; Ledwell et al. 2000; Scott et al. 2011; Nikurashin and Ferrari 2011; Brearley et al. 2013; Zemskova and Grisouard 2021; Evans et al. 2022). Given that mixing and dissipation patterns directly affect the transport of heat, freshwater, dissolved gases, and other tracers in the global ocean, as well as upwelling in the deep branches of the abyssal circulation (De Lavergne et al. 2016; Ferrari et al. 2016; MacKinnon et al. 2017; Polzin and McDougall 2022), an understanding of these processes is necessary to fully grasp global ocean dynamics.

[©] Supplemental information related to this paper is available at the Journals Online website: <https://doi.org/10.1175/JPO-D-24-0139.s1>.

Corresponding author: Tomas Chor, tchor@umd.edu

¹ Exceptions that resolve turbulent dynamics in similar configurations are the line of papers by Puthan et al. (2020), which focuses on different processes than those investigated here.

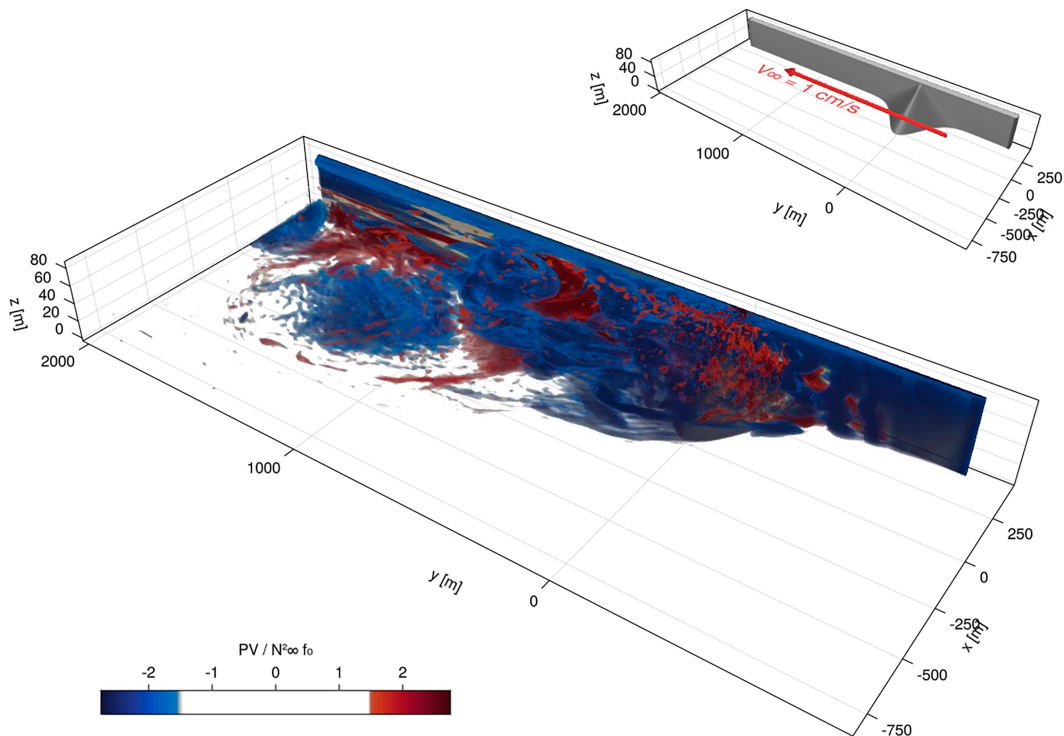


FIG. 1. Snapshot of Ertel PV in one of the simulations ($\text{Ro}_h = 1.25$ and $\text{Fr}_h = 0.08$) used in this paper. The inset shows a schematic of the configuration: a flow with initially constant-velocity upstream interacting with a headland, leading to a submesoscale wake. Here, west/east corresponds to the negative/positive x direction, and south/north corresponds to the negative/positive y direction. An animated version of this figure can be found in the online supplemental material.

contribution of flow–bathymetry interactions remains a source of uncertainty in global energy budgets (Ferrari and Wunsch 2009).

The broad goal of this study is to shed light onto some of the aforementioned points. Namely, we focus on the small-scale dynamics (i.e., turbulence) and energetics of flow interacting with headlands, with the expectation that some of the findings may also apply to more general bathymetric obstacles. In addition to the important role played by small-scale turbulence in mixing and dissipating, previous work has shown that they may be necessary to realistically represent the evolution of submesoscale instabilities and KE cascades (Jalali and Sarkar 2017; Chor et al. 2022), prompting us to employ large-eddy simulations (LESs) as the tool of choice. LESs resolve the relevant turbulent scales responsible for the forward KE cascade (Chamecki et al. 2019), allowing us to probe into processes that were absent in most previous investigations of this topic, which parameterized turbulence effects in a Reynolds-averaged Navier–Stokes (RANS) sense.

The paper is organized as follows. In section 2, we introduce the necessary theoretical background and details of our LES model and simulations. We start with an overview of the parameter space and dynamical regimes in section 3 and then move on to investigate their bulk properties in section 4. We focus on the submesoscale dynamics observed in some of the parameter spaces in section 5, specifically centrifugal–symmetric instabilities. We discuss our results in a broader context in section 6 and make final remarks in section 7.

2. Problem setup

a. Theoretical background

We study the problem of a constant barotropic flow interacting with a headland-like topographic obstacle, as depicted in Fig. 1 (details about the geometry are given in section 2b). We chose to focus on an anticyclonic interaction since, on average, it generates negative potential vorticity (Gula et al. 2016), and hence it is expected to be more unstable to submesoscale instabilities (see section 5) but also show results for its cyclonic counterpart whenever relevant. To make the numerics tractable, we use a relatively small domain and assume dynamic similarity, matching relevant nondimensional parameters with representative values for the real ocean. We also assume that we reach a sufficiently high Reynolds number such that the flow dynamics are self-similar (i.e., scaling up the simulation grid in size while keeping all dimensionless numbers constant would produce the same result). One consequence of this is that the (attached) bottom boundary layer (BBL) thicknesses need to be much smaller than the size of the obstacle. In the present case, the BBL is smaller than 10 m on average in all simulations, which, relative to the 80-m-tall headland, is consistent with observed flow–topography interactions (Nagai et al. 2021). Note also that experimentation with different values of roughness length scale for the bathymetry bottom drag (which directly affects the BBL thickness) produced virtually identical results (see details about the

TABLE 1. Parameters for the simulations used in this work.

L_x	1200 m
L_y	3000 m
L_z	84 m
Upstream velocity (V_∞)	1 cm s ⁻¹
Roughness length scale (z_0)	10 cm
Nudging layer length	300 m
Nudging rate at reentry	0.001 s ⁻¹
Headland horizontal length scale (L)	200 m
Headland vertical length scale (H)	40 m
Headland slope (α)	0.2
Headland Rossby number ($\text{Ro}_h = V_\infty/fL$)	(0.08, 0.2, 0.5, 1.25)
Headland Froude number ($\text{Fr}_h = V_\infty/N_\infty H$)	(0.08, 0.2, 0.5, 1.25)
Headland slope Burger number ($S_h = \text{Ro}_h/\text{Fr}_h$)	(0.064, 0.16, 0.4, 1, 2.5, 6.25, 15.625)
f -plane frequency (f)	(6.25, 2.5, 1, 0.4) $\times 10^{-4}$ s ⁻¹
Buoyancy frequency at the inflow (N_∞)	(3.125, 1.25, 0.5, 0.2) $\times 10^{-3}$ s ⁻¹

boundary conditions in section 2b). Thus, we ignore differences related to the finite Reynolds number and roughness length scale [consistent with previous investigations (Jalali and Sarkar 2017; Perfect et al. 2018)].

The relevant dimensional parameters for the configuration are then the headland horizontal and vertical length scales L and H , the Brunt–Väisälä frequency far from the obstacle N_∞ , the Coriolis frequency f , and the velocity of the upstream barotropic flow V_∞ (see Table 1 for the values used). This allows us to form the relevant nondimensional parameters defining the parameter space for our setup: the headland Rossby number, headland Froude number, and bulk headland slope, respectively,

$$\text{Ro}_h = \frac{V_\infty}{Lf}, \quad (1)$$

$$\text{Fr}_h = \frac{V_\infty}{HN_\infty}, \quad (2)$$

$$\alpha = \frac{H}{L}. \quad (3)$$

We also define the headland slope Burger number $S_h = \alpha N_\infty/f$ which in our configuration can be written as

$$S_h = \frac{N_\infty H}{fL} = \frac{\text{Ro}_h}{\text{Fr}_h}. \quad (4)$$

The term S_h captures the competition between the vertical decoupling effect of stratification and vertical organization effects of rotation and is expected to predict dynamical features of the flow such as wake separation (Magaldi et al. 2008) and vertical coupling of vortices (Perfect et al. 2018; Srinivasan et al. 2019). Note that S_h is equivalent to the square root of the Burger number as defined in some previous investigations (Magaldi et al. 2008; Perfect et al. 2018, 2020a).

Note that there are dynamical similarities between flows past headlands and the more recently studied problem of flows past seamounts, and indeed, we find that several behaviors observed in previous seamount studies qualitatively apply here (Perfect et al. 2018; Srinivasan et al. 2019; Perfect et al. 2020a), although there are also important differences (see section 3).

In particular, the presence of an east (positive x direction) wall makes it easier for flow to follow bathymetry and imposes a no-flow boundary condition. The latter not only makes the headland an inherently asymmetric problem but may also significantly change the form drag compared to a seamount, which dominates over skin drag in similar configurations (Edwards et al. 2004; Magaldi et al. 2008).

b. Numerical setup

We use the Julia package Oceananigans (Ramadhan et al. 2020) to run a series of LESs, which are performed by solving the filtered nonhydrostatic incompressible Boussinesq equations:

$$\frac{\partial \mathbf{u}}{\partial t} + \mathbf{u} \cdot \nabla \mathbf{u} + f \hat{\mathbf{k}} \times \mathbf{u} = -\nabla p - f V_\infty \hat{\mathbf{i}} + b \hat{\mathbf{k}} - \nabla \cdot \boldsymbol{\tau}, \quad (5)$$

$$\frac{\partial b}{\partial t} + \mathbf{u} \cdot \nabla b = -\nabla \cdot \boldsymbol{\lambda}, \quad (6)$$

where $\hat{\mathbf{i}}$ and $\hat{\mathbf{k}}$ are the unit vectors in the cross-stream x and vertical z directions, $\mathbf{u} = (u, v, w)$ is the three-dimensional velocity vector, b is the buoyancy, p is the modified kinematic pressure (Chamecki et al. 2019), $\boldsymbol{\tau}$ is the subgrid-scale (SGS) stress tensor, and $\boldsymbol{\lambda}$ is the SGS buoyancy flux. The term $f V_\infty \hat{\mathbf{i}}$ is a geostrophic pressure gradient force. For all simulations in this work, $\boldsymbol{\tau}$ and $\boldsymbol{\lambda}$ are modeled using a constant-coefficient Smagorinsky–Lilly closure (Lilly 1962; Smagorinsky 1963), and we mention that tests with the anisotropic minimum dissipation closure (Rozema et al. 2015; Vreugdenhil and Taylor 2018) produced similar results.

Oceananigans solves these equations using a finite-volume discretization, and we use a fifth-order weighted essentially nonoscillatory advection scheme and a third-order Runge–Kutta time-stepping method. The grid spacing is approximately 0.6 m vertically and 2 m in the streamwise y direction. For the x spacing, we hold the spacing approximately constant at 1.6 m in the headland region ($x \gtrsim -200$) and progressively stretch it to around 16 m at the west (negative x direction) wall. The upstream velocity, domain geometry, and bathymetry are held constant throughout all simulations.

The simulations aim to represent a constant-velocity, barotropic flow interacting with a headland, as depicted in Fig. 1,

which produces anticyclonic vorticity—a common feature along coastlines (Molemaker et al. 2015; Gula et al. 2016). To achieve that, all simulations are bounded in the x and z directions and periodic in the y (downstream) direction. The simulation is initialized with a uniform y -direction velocity $V_\infty = 0.01 \text{ m s}^{-1}$ and a uniform stratification N_∞^2 . The first 300 m of the domain in the (periodic) y direction nudges the flow back to $u = w = 0$, $v = V_\infty$, and $b = N_\infty^2 z$, making the y direction act like an inflow boundary condition upstream from the headland and an open boundary condition downstream from it. Due to computational constraints, we keep the topographic slope $\alpha = 0.2$ constant throughout all simulations and explore the parameter space (depicted in Fig. 2) by changing the Coriolis frequency f and the stratification N_∞^2 in each simulation, therefore varying Ro_h and Fr_h . Note that a slope of $\alpha = 0.2$, although considered steep in an ocean context, is still found in both seamounts [see data by Kim and Wessel (2011)] and coastal features [e.g., the California coast (Dewar et al. 2015)].

The headland is idealized as the following geometry:

$$\eta(z) = 2L\left(1 - \frac{z}{2H}\right), \quad (7)$$

$$h(y, z) = 2L - \eta(z)\exp\left\{-\left[\frac{2y}{\eta(z)}\right]^2\right\}, \quad (8)$$

such that the interior of the headland is defined as locations where $x > h(y, z)$. Equation (8), along with the parameters listed in Table 1, results in the geometry depicted in Fig. 1 (the nudging layer is not shown). Note that we span a wide range of slope Burger number values, including up to $S_h \approx 15$, which is somewhat higher than generally found in oceanic surveys (Lentz and Chapman 2004), but consistent with prior numerical work (Perfect et al. 2020a; Srinivasan et al. 2019), and can thus be interpreted as an upper bound for ocean values.

The boundary conditions for buoyancy in x and z are those of zero flux. The momentum boundary conditions are free slip at the top and bottom and on the west and east walls but follow a quadratic log law at the bathymetry implemented according to Kleissl et al. (2006), leading to a quadratic drag coefficient of 0.12. Note that we have experimented with different boundary conditions for the east wall and bathymetry and found that they do not significantly affect our results,² most likely due to a dominance of the baroclinic torque term in generating vorticity (Puthan et al. 2020). Thus, we chose to use no-flux conditions to avoid introducing shears from a vertical wall into the flow given that vertical walls are extremely rare in the ocean.

² While Puthan et al. (2020) found that dynamics can be sensitive to bottom boundary conditions, we found that our results were unchanged as long as the bathymetry had a quadratic drag law. This includes changes to the roughness length, which did not significantly affect results when values were between $\mathcal{O}(0.1)$ and $\mathcal{O}(1)$ m (values outside this range were not tested). We have not tested no-slip boundary conditions as the LES technique implies viscous layers that are much smaller than the grid scale, making such a boundary condition inappropriate for our case.

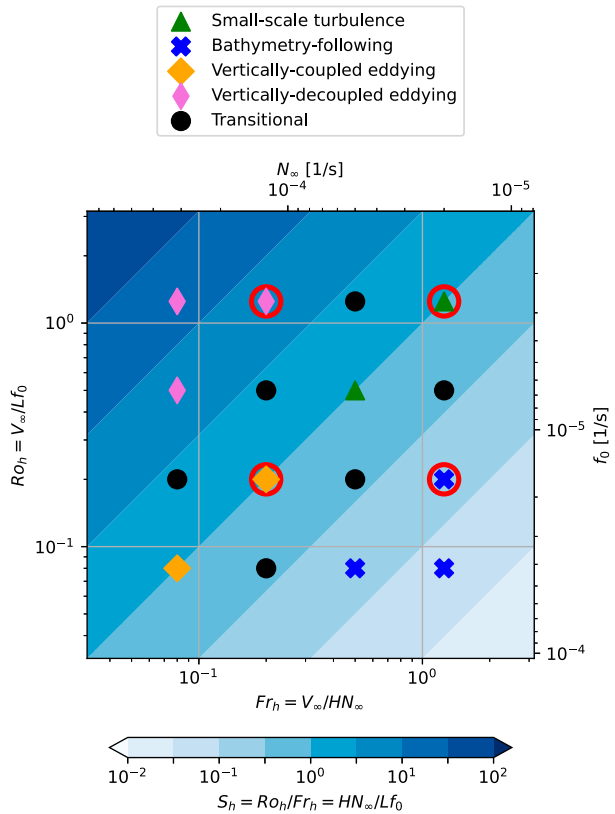


FIG. 2. The Ro_h - Fr_h parameter space considered in this work where each point corresponds to a different simulation. Points are color and shape coded according to their regime. Background colors indicate the equivalent slope Burger number S_h . Simulations circled in red are shown in Figs. 3–5.

The bathymetry in our simulations is represented numerically using a full-step immersed boundary method, and it was verified to produce virtually identical results to the partial-step method (Adcroft et al. 1997) for the resolutions used in this paper. That said, given that the slopes at the grid scale are not preserved with this implementation, we exclude the first few points adjacent to the topography from analyses, focusing instead on the interior outside of the bottom boundary layer. Results were found to be numerically converged by Ozmidov scale analysis and auxiliary runs with different domain dimensions and spacings (see appendix A). All simulations are allowed to spin up for 20 advective periods (defined as $T = L/V_\infty$), and all analyses are done in the subsequent $50T$ period.

3. Overview of dynamics

As a high-level description, in all cases, the interaction with the headland creates anticyclonic vorticity and turbulence, which can be seen in Fig. 3 for four simulations. Note that the approximate minima of the anticyclonic vorticity in the wake coincide with about 5–10 times the value of Ro_h , putting the values of Ro_h considered here in the submesoscale range for most simulations. Although the aforementioned description is valid for all simulations, Fig. 3 also shows that the flow

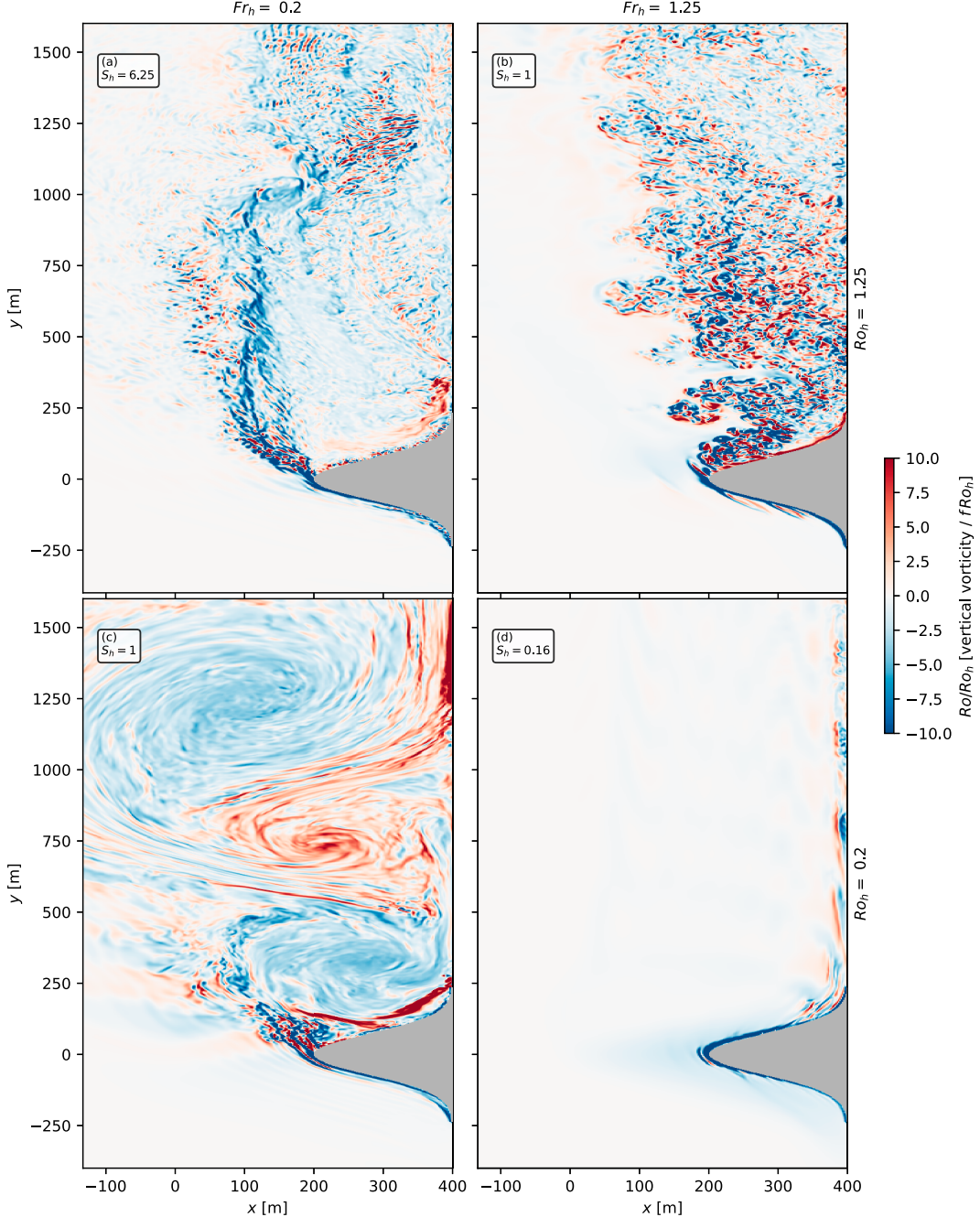


FIG. 3. Horizontal cross sections of pointwise Rossby number Ro divided by Ro_h at middepth for four selected simulations (corresponding to points with red circles in Fig. 2), each representative of a different regime. The shaded gray area corresponds to the headland, and the mean flow ($V_\infty = 0.01 \text{ m s}^{-1}$) is directed northward (i.e., positive y direction). An animated version of this figure can be found in the supplemental material.

behavior after the initial topographic interaction can be very different for different simulations, indicating the existence of different dynamical regimes.

We identified four such regimes within our simulations, and we show one representative case for each in Figs. 3–6. We find that S_h is a useful quantity to predict dynamical regime changes, and the regimes we find are generally consistent with comparable

ones described in previous headland literature (Magaldi et al. 2008)—apart from details of small-scale turbulence that were not previously resolved. We describe all regimes below, although we make no attempt to fully quantify the precise critical values of S_h at which transitions happen, as it is not in our scope and would require many more simulations. The four simulation regimes can roughly be described as follows:

- Bathymetry-following regime: For small S_h (Fig. 3d), we tend to not observe any wake separation, and the flow mainly follows the bathymetry, similar to quasigeostrophic dynamics (Pedlosky 1987). In this regime, the transition to turbulence is done by small-scale eddies in the bottom boundary layer likely created through a combination of boundary layer shear, downslope bottom flow due to Ekman transport, and boundary layer-scale centrifugal-symmetric instabilities (CSIs) (MacCready and Rhines 1991; Wenegrat and Thomas 2020). In this regime, we also observe evidence of internal waves (not shown), which have not been observed to break in any of the cases we simulated and therefore act to transfer energy out of the domain.
- Vertically coupled eddying regime: For flows with intermediate S_h values and $\text{Ro}_h \approx \text{Fr}_h \lesssim 0.2$, eddies form at the tip of the bathymetry and occasionally drift away as isolated features, as seen in Fig. 3c. These eddies are mostly vertically coupled (i.e., low vertical shear; Perfect et al. 2018) as can be seen in Fig. 4c and quickly adjust the potential vorticity (PV) signature³ from negative at the headland tip to zero in the vortices (Fig. 5c). In addition to boundary layer eddies, we show that CSIs likely play a role in the wake dynamics in simulations in this regime with high enough Ro_h (see section 5).
- Vertically decoupled eddying regime: For larger values of S_h (Fig. 3a), there tends to be a clear vortical wake, often (for large enough Ro_h) maintaining a negative PV signature long downstream from the headland tip. Although, it is apparent that the magnitude of the negative PV signal decreases as the flow moves downstream from the headland tip, which we show in section 5 to be due to CSIs (see Fig. 5a). Furthermore, there is evidence of substantial upscale energy cascade, resulting in wake vortices that are significantly larger in size in comparison to the headland dimensions. Importantly, for this regime, the decoupling of vertical levels due to stratification effects creates significant vertical shear (see Fig. 4a; Perfect et al. 2018).
- Small-scale turbulence regime: If both rotation and stratification are weak (i.e., $\text{Ro}_h \gtrsim 0.5$ and $\text{Fr}_h \gtrsim 0.5$), the flow produces a wake without any discernible roll-up or dynamical structures at the scale of the headland or larger, suggesting the absence of any kind of upscale energy cascade. The wake is then characterized by small-scale turbulence features as seen in Figs. 3b and 5b. Investigations of this regime are more common in the atmospheric sciences literature (Belcher and Hunt 1998; Finnigan et al. 2020).

Note that in addition to submesoscale flows, the parameter space range explored here also produces flow behaviors qualitatively similar to mesoscale (e.g., the bathymetry-following regime) and small-scale flows (small-scale turbulence regime). This wide range of regimes ensures that several routes from mean flow to turbulence are present in our simulations. We also note that, similarly to our configuration, S_h can predict the

³ Whenever appropriate, the Ertel PV used in the calculations follows the filtering procedure proposed by Bodner and Fox-Kemper (2020) using a filter scale of 15 m (although we observed the results to not be sensitive to the precise choice of scale).

transition between a vertically coupled and vertically decoupled regime for isolated seamounts (Perfect et al. 2018; Srinivasan et al. 2019) despite the difference in geometry.

As a point of comparison, we can connect our results to those of Gula et al. (2016), who modeled a more realistic headland system using the Regional Ocean Modeling System (ROMS; Shchepetkin and McWilliams 2005). Focusing on the headland at the Great Bahama Bank (at the southwestern corner of their Fig. 2), we can use their figures along with topography data to estimate: $L \approx 6$ km, $H \approx 400$ m, $N_\infty^2 \approx 10^{-4}$ s⁻², $f \approx 6.6 \times 10^{-5}$ s⁻¹, and $V_\infty \approx 1$ m s⁻¹. These values indicate that, for their headland, $\text{Ro}_h \approx 2$ and $\text{Fr}_h \approx 0.2$, being therefore in the vertically decoupled eddying regime (albeit with a shallower bulk slope than the one used here). Comparing our Fig. 3a ($\text{Ro}_h = 1.25$ and $\text{Fr}_h = 0.2$) with their Fig. 1b, we see a similar downstream eddy roll-up, with our simulation expectedly resolving the vertical vorticity at much smaller scales, accordingly reaching larger magnitudes of Ro. The difference in the PV signature seen at different depths in their Fig. 2 also indicates vertical decoupling of layers, which again is in line with expectations from the present work. These agreements suggest that the dynamics obtained in our idealized headland model are representative of dynamics obtained with realistic topography.

Finally, although the range of parameter space considered in this study is large, one can anticipate that other regimes may happen that are not present here. For example, for high enough Ro_h , the growth rate of CSIs (see section 5) will be slow compared to other shear instabilities in the flow (Haine and Marshall 1998), while for low enough Ro_h , the drag exerted by the headland may not be enough to produce a negative PV signature at all in the flow. Both cases may result in different dynamics from the ones described here. However, we believe the parameter space spanned here (Table 1) encompasses most oceanographically relevant values.

A useful way to visualize turbulent flow is to focus on the KE dissipation rate:

$$\varepsilon_k = 2\nu S_{ij} S_{ij}, \quad (9)$$

where ν is the subgrid-scale viscosity and $S_{ij} = (\partial u_i / \partial x_j + \partial u_j / \partial x_i) / 2$ is the strain rate tensor. Time averages (indicated throughout as $\bar{\cdot}$) of ε_k are shown in Fig. 6. The difference in distribution of $\bar{\varepsilon}_k$ between simulations is clear, with some simulations dissipating KE only in the boundary layer attached to the bathymetry (specifically simulations in the terrain-following regime, exemplified in Fig. 6d), while other simulations dissipate most of their KE in the wake (as is the case for simulations in the vertically decoupled eddying regime, exemplified in Fig. 6a). We can further inspect results by averaging⁴ $\bar{\varepsilon}_k$ in the vertical

⁴ Note that, as mentioned in the text, when integrating or averaging results spatially, we ignore points that are within approximately 5 m from the headland. This is done in order to avoid contamination of the results with unresolved dynamics, since these points are numerically affected by the wall model and the immersed boundary discretization.

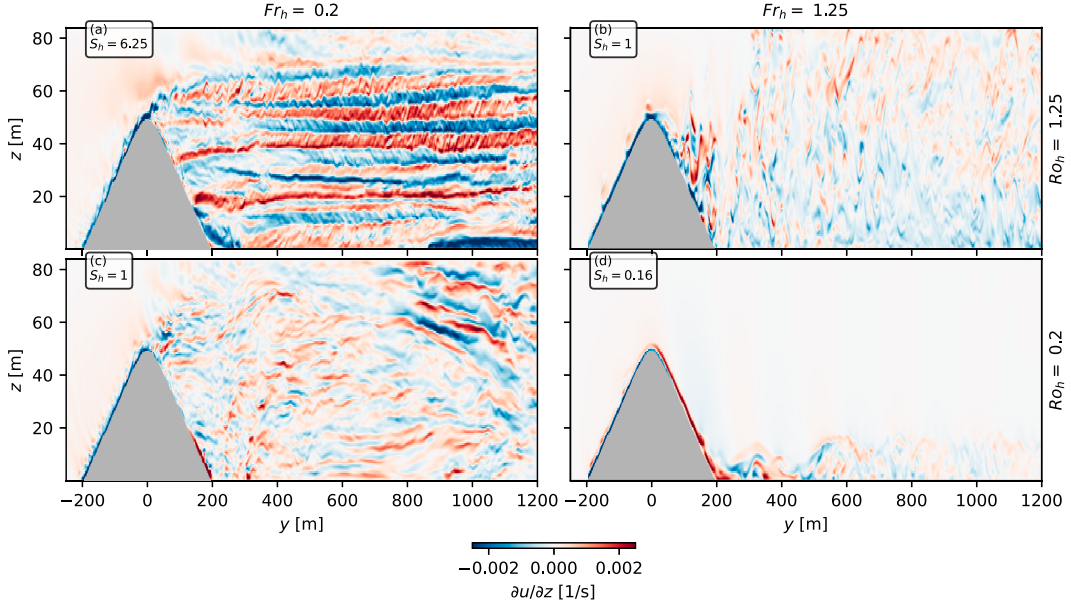


FIG. 4. Vertical cross sections of u -direction vertical shear at approximately $x \approx 245$ m for the same four simulations shown in Fig. 3. The flow is moving from left to right in the panels.

and cross-stream directions $\langle \bar{\varepsilon}_k \rangle^{xz}$ for all simulations, which is shown in Fig. 7a (each curve corresponds to a different simulation, and they are color coded based on S_h). Figure 7a makes it clear that the wake turbulence becomes progressively more important for the overall dissipation with increasing values of S_h , which is expected based on the increasingly important role of stratification (Srinivasan et al. 2019, their Fig. 15e). While the position of the secondary peak in KE dissipation downstream from the headland (in $S_h \gtrsim 1$ simulations) is likely affected by CSI dynamics, it results primarily from the wake roll-up in these simulations. This can be seen by comparing, for example, the location of peak dissipation for simulations with $S_h \approx 6.25$ ($y \approx 500$ m) with the location in Fig. 7a where the turbulent wake is the widest (also $y \approx 500$ m) and likewise for other simulations.

We can perform a similar quantification for the buoyancy mixing rate ε_p , which we approximate as

$$\varepsilon_p = \kappa_b \frac{\nabla b \cdot \nabla b}{N_\infty^2}, \quad (10)$$

where κ_b is the subgrid-scale diffusivity using a Prandtl number of unity. In previous tests by the authors (using a similar domain but without a nudging layer or boundary fluxes), Eq. (10) proved to be a good approximation of the exact equation for the buoyancy mixing rate, which uses the stratification of the sorted buoyancy field (see Winters et al. 1995; Umlauf et al. 2015 for details). Figure 7b shows the x -, z -, and time-averaged buoyancy mixing rate as a function of downstream distance. The similarity with the KE dissipation rate curves in Fig. 7a is clear, although ε_p values are smaller by a factor of approximately 5, indicating a mixing efficiency of $\gamma = \varepsilon_p / (\varepsilon_k + \varepsilon_p) \approx 0.2$ that is roughly constant throughout the

wake (except very close to the bathymetry)—in accordance with standard values for γ (Gregg et al. 2018; Caulfield 2021). We note the elevated mixing rate in the wake differs from the behavior proposed by Armi (1978), who suggested that mixing happens only along boundaries and well-mixed waters are transported into the interior. In all our simulations with eddying wakes, a nonnegligible amount of mixing happens after the flow detaches from the boundary.

4. Energetics and bulk results

Understanding the influence of stratification and rotation on bulk quantities can aid both future parameterization efforts and attempts at global energy budgets. Therefore, we dedicate this section to investigating bulk quantities in our simulations with a focus on flow energetics. To make our results easily scalable, we normalize them here using the external scales for velocity and length: V_∞ and L . This normalization was found to be accurate by rerunning all simulations in this paper with different values of V_∞ and observing that the normalized results remained largely unchanged.

We start by investigating the volume-integrated, time-averaged normalized KE dissipation rate:

$$\bar{\varepsilon}_k = \frac{\iiint \bar{\varepsilon}_k dx dy dz}{V_\infty^3 L H}, \quad (11)$$

where the normalization comes from assuming $\varepsilon_k \sim V_\infty^3/L$ and $\iiint (\cdot) dx dy dz \sim L^2 H$, and results are shown as a function of the slope Burger number S_h in Fig. 8a. Each point corresponds to a different simulation, and the organization as a linear function of S_h (shown as a dashed line for reference) is striking. These results, for simulations spanning a range of

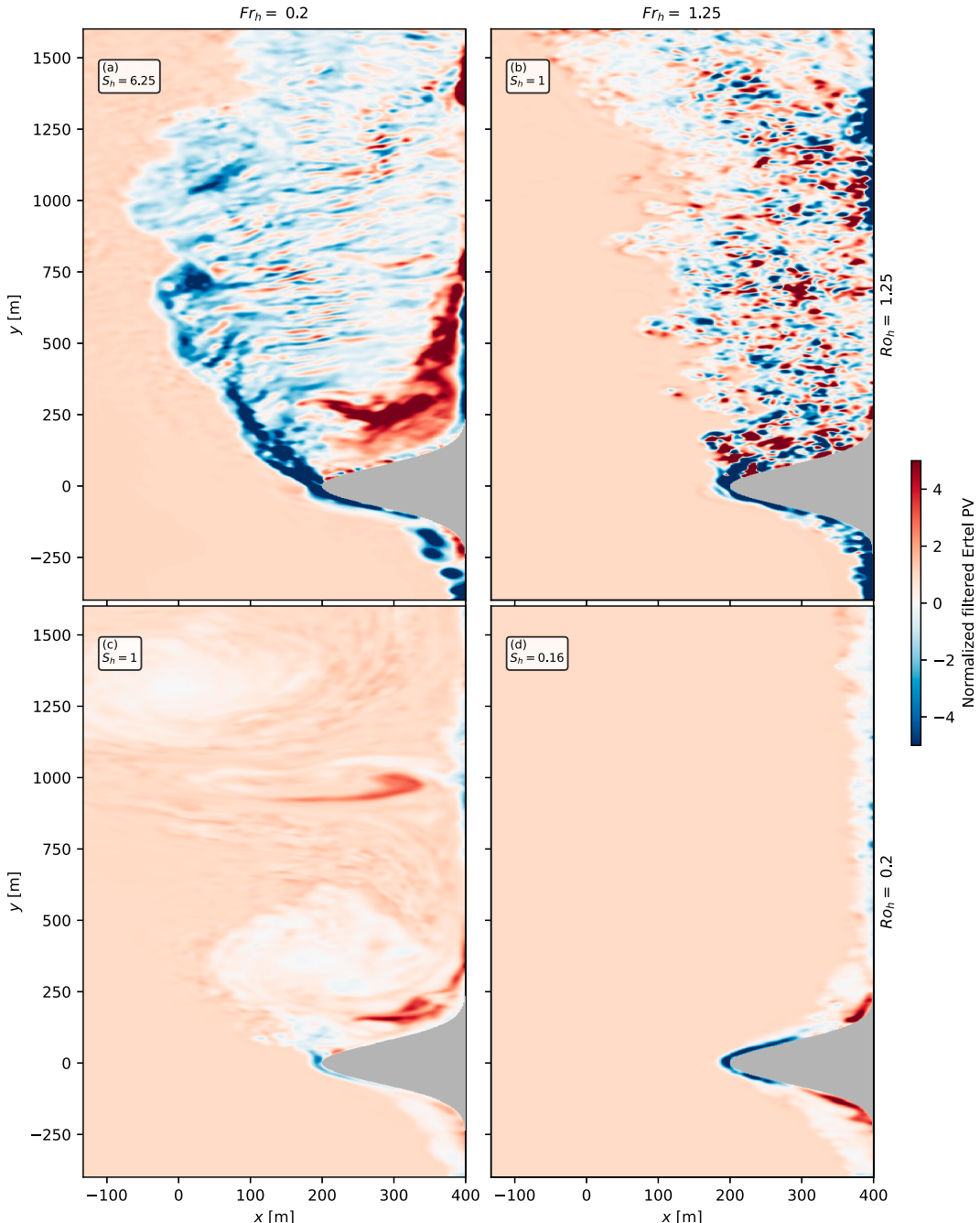


FIG. 5. As in Fig. 3, but showing filtered Ertel PV [$\nabla \tilde{b} \cdot (\nabla \times \tilde{\mathbf{u}} + f\hat{\mathbf{k}})$] normalized by $N_\omega^2 f$, where $\hat{\mathbf{k}}$ is the unit vector in the vertical direction and $\tilde{\cdot}$ indicates a horizontal filtering operation at the scale of 15 m.

different dynamical regimes and physical processes generating cross-scale energy transfers (see section 3), indicate that the bulk effects of small-scale turbulence seem to follow a general relationship regardless of specific regimes, suggesting that the details of the dynamical routes to turbulence may not be critical to determining the bulk turbulent energetics. Such a conclusion is different from the picture that has emerged based on upper-ocean investigations, where the flow dynamics and routes to turbulence seem to significantly impact energetics

(see section 7 for a discussion). However, results consistent with ours, although not interpreted in this way, can be found in previous work on flow–bathymetry interactions. Specifically, Srinivasan et al. (2019) reported that ε_k is inversely correlated with Froude number and Srinivasan et al. (2021) reported it being correlated with Rossby number.

A complete analysis of the turbulent KE (TKE) budget across simulations spanning such a wide range of regimes, leading to a full explanation for the relationship seen in

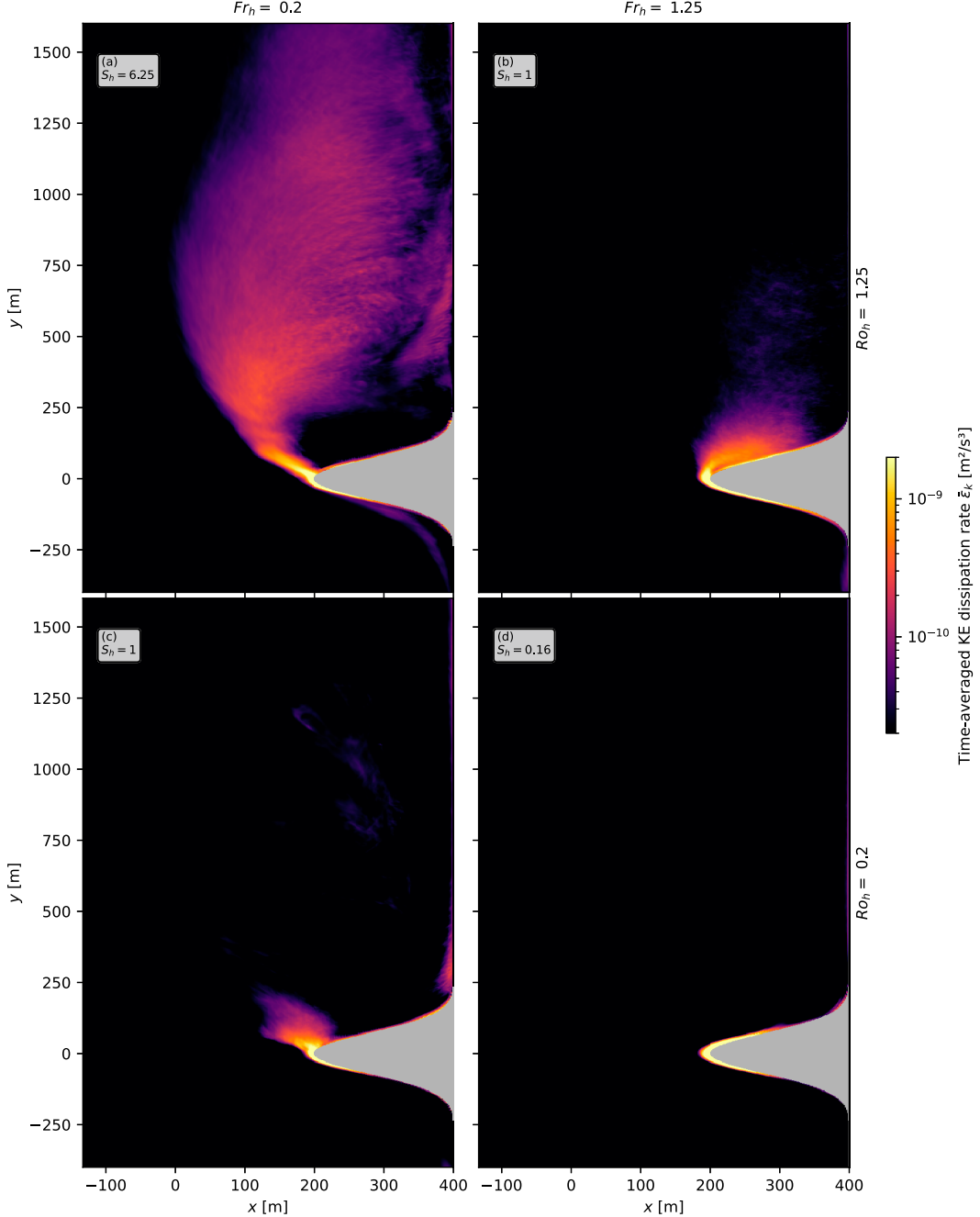


FIG. 6. As in Fig. 3, but showing the time-averaged KE dissipation rate $\bar{\epsilon}_k$.

Fig. 8a, is outside the scope of this work. However, we note that such an organization may be partly explained by the internal form drag, which captures effects of lee waves and eddies that are formed and shed from bathymetry (Magaldi et al. 2008, section 3.3). Form drag is important for flows impinging on obstacles (McCabe et al. 2006; Warner and MacCready 2009, 2014), and although it does not exert work on the fluid as a whole (Gill 1982; MacCready et al. 2003), it represents a transfer of energy from the barotropic flow into the baroclinic flow, which subsequently can be a source of TKE and

dissipation. We calculate the normalized integrated form drag work \mathcal{D} as (Warner and MacCready 2014)

$$\mathcal{D} = -\frac{1}{V_\infty^3 LH} \int \int \bar{p}_b \partial_y h dx dy, \quad (12)$$

where \bar{p}_b is the time-averaged kinematic pressure at the bottom and $\partial_y h$ is the alongstream bathymetry slope. The term \mathcal{D} is shown in Fig. 8b, and it is apparent that, for most of the parameter space, the drag work also organizes approximately

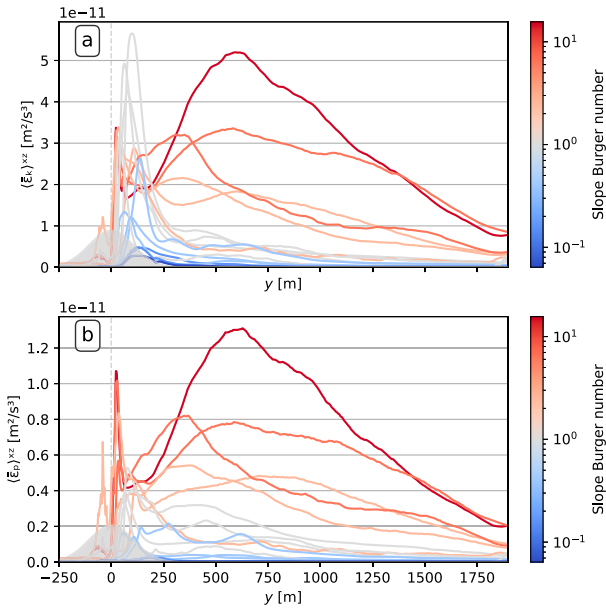


FIG. 7. (a) The x , z , and time averages of KE dissipation rate as a function of downstream distance y for all simulations. (b) As in (a), but for buoyancy mixing rate. Each curve is color coded according to its respective simulation's headland slope Burger number S_h . Note that the 5 m closest to the headland is excluded in this average to avoid potential contamination of results by the immersed boundary discretization.

linearly with S_h . A reasonable hypothesis based on these results is that the overall pattern of organization of ε_k with S_h stems from the approximately linear relationship between drag work and S_h , indicating an energy transfer from the barotropic flow into dissipation (such that $\varepsilon_k \approx 0.1\mathcal{D}$ for most simulations based on Fig. 8).

However, we also note that the form drag work \mathcal{D} levels out for high values of the slope Burger number S_h (particularly in the vertically decoupled eddying regime, depicted as magenta diamonds). While this is qualitatively consistent with previous work on form drag [see, e.g., Eq. (68) of Teixeira (2014) and Fig. 12 of Magaldi et al. (2008)], it does not happen for ε_k , indicating that the increasing trend for dissipation at large S_h seen in Fig. 8a may not be fully attributable to a simple increase in \mathcal{D} . In fact, throughout our simulations, we find that advection of KE, buoyancy fluxes, pressure transport, and geostrophic pressure work are all important, signaling that a complete explanation of the trend for ε_k likely involves a complex interaction between all these processes.

A linear organization with S_h is also observed for the normalized buoyancy mixing rates \mathcal{E}_p [defined similarly to Eq. (11) in Fig. 9a]. Consistent with Fig. 7, values of \mathcal{E}_p are smaller than ε_k by approximately fivefold, and the similarity between both results and the connection between the two processes suggests that both trends have a common explanation. Additionally, if one uses ε_p to define a buoyancy diffusivity, in such a way that it can be written in normalized form as

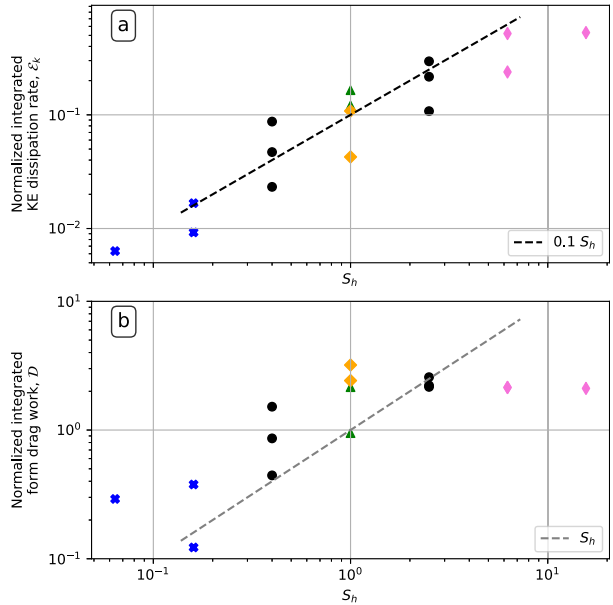


FIG. 8. Normalized volume-integrated, time-averaged quantities as a function of slope Burger number S_h . Points are color and shape coded as in Fig. 2. (a) KE dissipation mixing rate. (b) Form drag work [Eq. (12)]. Black and gray dashed lines are shown as references for $\sim S_h$.

$$\mathcal{K}_b = \frac{1}{V_\infty L^3 H} \frac{\iiint \bar{\varepsilon}_p dx dy dz}{N_\infty^2}, \quad (13)$$

then the linear scaling of ε_p with S_h implies

$$\mathcal{K}_b \sim \text{Ro}_h \text{Fr}_h. \quad (14)$$

Note that in deriving Eq. (13) we assume a scaling for the diffusivity of $V_\infty L$ and the choice of ε_p guarantees that only irreversible processes are considered. Results for \mathcal{K}_b can be seen in Fig. 9b as a function of $\text{Ro}_h \text{Fr}_h$, where the scaling of Eq. (14) is confirmed. This result contrasts with the steeper scaling found by Perfect et al. (2020a) of $\mathcal{K}_b \sim (\text{Ro}_h \text{Fr}_h)^2$ and is more in line with the recent result of Mashayek et al. (2024), which used hydrostatic simulations to arrive at a relatively shallow scaling.⁵

A comment on our choice to use ε_p in Eq. (13) is that, while using $\bar{w}'\bar{b}'$ as a proxy for irreversible buoyancy mixing is common, such an assumption is expected to be valid only under special circumstances (Peltier and Caulfield 2003; Gregg et al. 2018) which do not hold in our domain. Likely as a result of our open domain, coupled with the complex interaction of processes present throughout our parameter space, $\bar{w}'\bar{b}'$ is positive in most of our simulations—opposite to what is

⁵ Using our notation, Mashayek et al. (2024) obtained a scaling of $K_b \sim \text{Fr}_h^{1.7} \text{Ro}_h^{1.1}$, although direct comparisons with our results are challenging since they did not normalize their values or otherwise control for differences in topographic obstacle size and current velocity.

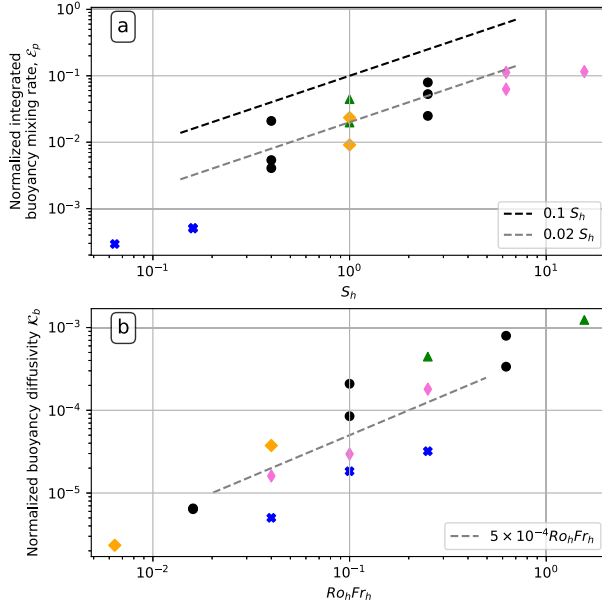


FIG. 9. (a) Normalized, volume-integrated, time-averaged buoyancy mixing rate. (b) Normalized diffusivity [calculated as in Eq. (13)] as a function of $Ro_h Fr_h$. Dashed back line is the same as in Fig. 8a, and gray lines are shown for reference. Points are color and shape coded as in Fig. 2.

usually expected—indicating a transfer of available potential energy into TKE. This fact highlights that one should exercise caution in using the (reversible) turbulent buoyancy flux as a proxy for irreversible mixing in flow-topography interactions. With that said, in those simulations where $w'b' < 0$, the scaling in Eq. (14) still holds for diffusivities calculated with the turbulent buoyancy flux (not shown here).

5. Presence of centrifugal-symmetric instabilities in the flow

In this section, we turn our attention to regimes that exhibit submesoscale structures in the wake: the vertically decoupled and vertically coupled regimes, as well as the transitional simulations in-between (see Fig. 2). We note that flows similar to those in the terrain-following regime in a similar part of parameter space have been studied in the past, albeit without the curvature introduced by the headland (Umlauf et al. 2015; Wenegrat et al. 2018; Wenegrat and Thomas 2020). Given the parameter space this regime lies in, the attached BBL may be expected to have CSIs (Wenegrat et al. 2018, their Fig. 19), but we do not have enough resolution in our configuration to study them in detail since they are confined within the boundary layer in this case.

A flow is unstable to CSIs when the normalized PV is negative, that is, when

$$\hat{q} = \frac{\nabla b \cdot (\nabla \times \mathbf{u} + f\hat{\mathbf{k}})}{N_{\infty}^2 f} < 0. \quad (15)$$

The reader is directed to previous works for further information about CSIs (Haine and Marshall 1998), and we limit

ourselves to mentioning that the linear growth rate of such instabilities can be expressed as⁶

$$\omega^2 \leq -f^2 \hat{q}, \quad (16)$$

and that, once active, CSIs will act to mix fluid until the PV signal reaches marginal stability ($\hat{q} = 0$) everywhere (Haine and Marshall 1998). Thus, the fact that initially negative PV wake signatures give way to zero PV downstream in many of our simulations is suggestive of CSI activity (see Figs. 5a,c), which is also in line with previous literature of flow interacting with bathymetry (Dewar et al. 2015; Molemaker et al. 2015; Gula et al. 2016; Srinivasan et al. 2019, 2021). Moreover, for values of \hat{q} present at the headland tip in our simulations, Eq. (16) indicates that CSIs should evolve at approximately inertial time scales (ranging from approximately 7 h for simulations with $Ro_h = 0.08$ to approximately 30 h for $Ro_h = 1.25$), reaching a fully developed state within a couple growth periods (Chor et al. 2022). Taking into consideration uncertainties due to a preexisting turbulent state at separation and due to topography-induced motion (e.g., accelerating flows at the headland tip and wake roll-ups), this evolution is consistent with the dynamics depicted in Fig. 5.

There is also visual evidence of CSIs, and we illustrate them with simulation $Ro_h = 1.25$ and $Fr_h = 0.2$ in Fig. 10, which shows the normalized (unfiltered) PV \hat{q} , KE dissipation rate ε_k , and streamwise vorticity ω_x . Figures 10a–i are placed progressively downstream, following the wake evolution. Each vertical cross section can be roughly divided into three regions: (i) the stratified interior, which can be seen at the top left (west) of each panel; (ii) the initially thin tilted strip resulting from the detached BBL, which is characterized mainly by its strong negative \hat{q} signature seen in Fig. 10a; and (iii) the region of return flow that is located between region ii and the east wall.

Focusing first on region ii, Fig. 10a shows that the headland BBL detaches as a strip of anticyclonic vorticity and negative PV, which is associated with high dissipation rates (Fig. 10d). Note that the BBL expands as it detaches from the headland (seen clearly in Fig. 10j), and its thickness is smaller than 10 m on average in all simulations. Further downstream, this detached BBL progressively develops into a thin braided strip (Figs. 10h,i) that progressively increases in horizontal size. This is the result of counterrotating, approximately flat motions (usually referred to in the literature as “cells”) that grow horizontally and develop small [$\mathcal{O}(5)m$] overturning instabilities oriented in the cross-stream direction (more clearly seen in the ω_y) which commonly accompany finite-amplitude CSIs [viz., Dewar et al. (2015), Chor et al. (2022) for a more in-depth discussion]. As this braided structure evolves, the PV in the strip progressively approaches marginal stability (Figs. 10b,c,j), in a signature typical of CSIs (Haine and Marshall 1998; Taylor and Ferrari 2009; Chor et al. 2022). Note that the overturnings are thought to be secondary Kelvin-Helmholtz

⁶ Here, we assume a uniform environment with buoyancy frequency N_{∞} for simplicity.

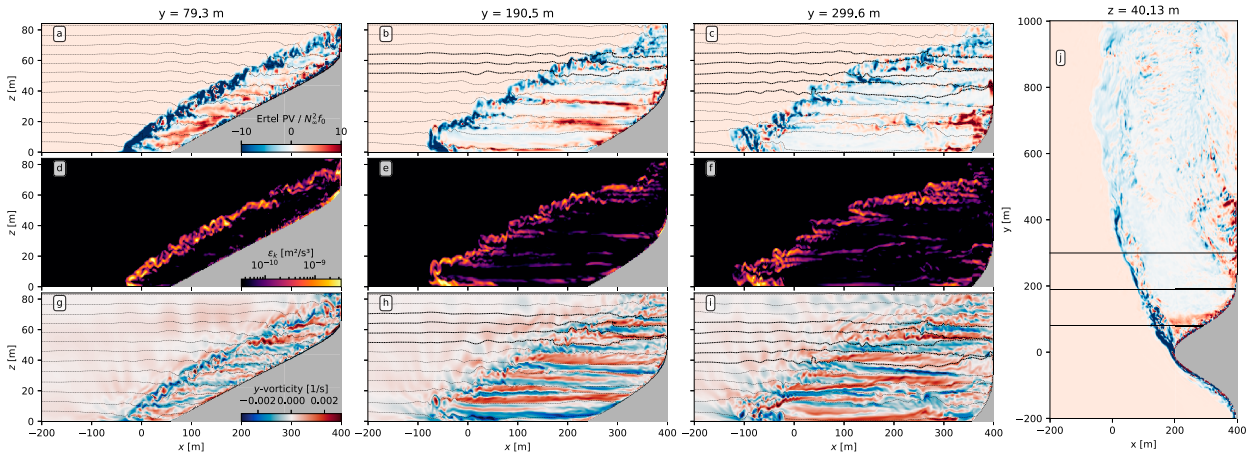


FIG. 10. Vertical cross sections at progressively increasing values of y from simulation with parameters $\text{Ro}_h = 1.25$ and $\text{Fr}_h = 0.2$. (a)–(c) Unfiltered normalized PV. (d)–(f) KE dissipation rates. (g)–(i) Streamwise vorticity. Dashed black lines represent isopycnals. (j) Horizontal cross section of unfiltered normalized PV at the same time as other panels. Solid black lines in (j) indicate locations of (a)–(i).

instabilities, again in line with CSI dynamics which produce them as the shear associated with the primary counterrotating cells gets large (Taylor and Ferrari 2009; Chor et al. 2022). Kelvin–Helmholtz billows generated directly from the headland shear (i.e., without CSIs) would be oriented in the along-stream direction, perpendicular to the overturnings shown in Fig. 10.

Starting at 200 m from the headland tip, regions ii (the detached BBL strip) and iii (the return flow) blend together, and it is challenging to accurately separate both. Nevertheless, it is apparent that region iii has some pockets of positive PV resulting from the return flow interacting with the bathymetry cyclonically (better seen in Fig. 10b), which gets mixed with negative PV (due to CSIs) to reach zero PV in most of this region. Notably, there are also horizontally large [$\mathcal{O}(200)\text{m}$] counterrotating cells in region iii (better seen in Figs. 10h–i) that are not generally associated with high dissipation rates or strong negative PV signals. We interpret them as mature CSI cells which have already mixed PV into a marginal stability

state and which are present close to the headland tip due to the return flow advecting them upstream.

The role of negative PV in creating CSIs can be made clearer when comparing the results in Fig. 10 with results from an identical simulation, but with opposite-sign Coriolis frequency, as shown in Fig. 11. A comparison between both figures confirms the significant difference in dynamics. The counterrotating cells and braids present in region ii of Fig. 10 cross sections are nowhere to be seen in Fig. 11. Instead, the detached BBL, which now has a positive \hat{q} signature, approximately maintains its shape as it travels downstream (Figs. 11a–c,j). Accordingly, KE dissipation rates for region ii of the cyclonic case decrease much faster as the flow travels downstream than for the anticyclonic case (cf. Figs. 11d–f with the same panels of Fig. 10), consistent with a lack of CSIs extracting energy from the flow. This results in a value of the normalized dissipation rate \mathcal{E}_k for the cyclonic simulation that is lower than for the anticyclonic simulation by approximately tenfold (see appendix B for a comparison of bulk results

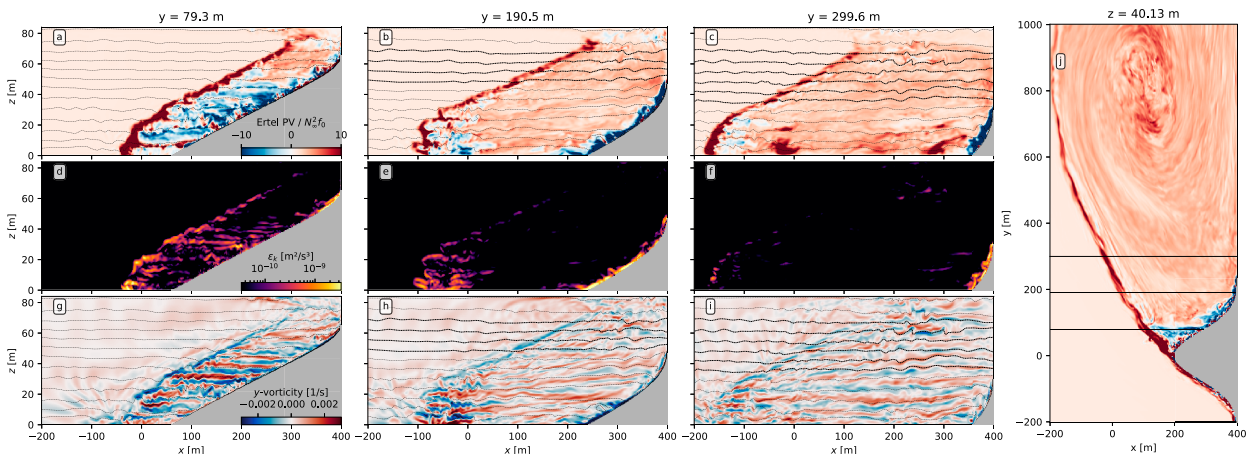


FIG. 11. As in Fig. 10, but with opposite sign f .

between anticyclonic and cyclonic configurations). The only place we see evidence of CSIs (as in counterrotating cells or braids with high dissipation rates which create overturning motions) is in pockets of negative PV that are present in region iii as a result of the return flow interacting anticyclonically with the headland. Correspondingly, since there are fewer instances of CSI in the cyclonic headland interaction, we see weaker mature CSI cells in region iii.

Comparing the horizontal cross sections (panel j) between Figs. 10 and 11, the difference in wake mixing also becomes clear, since the anticyclonic wake rapidly adjusts to a zero-PV state, while the cyclonic wake retains its shape and PV signal much more coherently, creating a large coherent eddy. The dynamics just described, and especially dynamical differences between the anticyclonic and cyclonic headland interactions, point toward CSIs being present and active in the wake of these simulations. They are present from the headland tip onward for the anticyclonic case in Fig. 10 and, to a lesser extent, in localized pockets of negative \hat{q} for the cyclonic case in Fig. 11. While we illustrated both anticyclonic and cyclonic dynamics here with simulation $\text{Ro}_h = 1.25$ and $\text{Fr}_h = 0.2$, the comparisons done in this section (as well as the criterion examination) were repeated for all our simulations, by which we were able to confirm that CSI-producing dynamics happen in all simulations where there is an eddying wake with a negative \hat{q} signal at the headland tip. This includes all simulations in the vertically decoupled eddying regime, one of the simulations in the vertically coupled eddying regime, and all transitional simulations in between. Appendix C presents a similar analysis for a simulation in the vertically coupled eddying regime for comparison.

It is useful to once again check our results against the simulation with realistic bathymetry from Gula et al. (2016), which we estimate to have $\text{Ro}_h \approx 2$ and $\text{Fr}_h \approx 0.2$ (see section 3 for details). The simulation shown in Fig. 10 ($\text{Ro}_h = 1.25$, $\text{Fr}_h = 0.2$) is the simulation that most closely matches these parameters. We observe that, in addition to the PV patterns in Fig. 10j matching the patterns seen in Fig. 2 of Gula et al. (2016), the meandering structures in our vertical cross sections also match similar structures in their Figs. 3g and 3h, but with smaller-scale meanders and overturning motions due to increased resolution.

Given that CSIs can behave differently depending on if they are dominated by centrifugal modes (horizontal shear) or symmetric modes (vertical shear) (Chor et al. 2022), it is useful to characterize where they lie in this spectrum. One common way to do this is by comparing the contributions of the horizontal and vertical components to the total PV. For centrifugally dominated CSIs, the vertical vorticity term $1 + \text{Ro}$ [i.e., the contribution from the vertical component in Eq. (15)] is expected to dominate, while the other components dominate for symmetric modes. We show both the total and vertical vorticity term contributions to PV in Fig. 12 for three simulations with $\text{Fr}_h = 0.08$. It is clear that the vertical component dominates the PV signal, with most of the differences owing to the small-scale Ro distribution (which is not present in the filtered PV by construction), suggesting that centrifugal modes dominate these simulations. Figure 12 also indicates that, in general, for the headlands in the parameter

space range considered here, accurately estimating Ro (which has significant contributions from both along- and across-stream gradients) is key for determining the sign of the full Ertel PV.

Another important quantity for CSI energetics is the shear production rate Π , calculated as

$$\Pi = -\bar{u}'_i u'_j \partial_j \bar{u}_i, \quad (17)$$

where u'_i indicates a departure from the time average \bar{u}_i . The term Π is shown in Figs. 13a–c for three simulations. Note that CSIs are expected to be growing primarily within regions enclosed by the dashed green line (which indicates negative average PV); however, there are significant rates of shear production throughout most of the domain for these simulations. In fact, while CSIs start growing after BBL separation at the headland tip in all simulations analyzed in this section, Fig. 13 suggests that their contributions to the total energetics may be relatively small for flows with low slope Burger number S_h (Fig. 13a), while the opposite is true for large S_h (Fig. 13c). Note, however, that while Π is negative in some regions, indicating an upward KE cascade (likely due to eddy roll-ups), it is mostly positive in regions where CSIs are expected, which reflects the ability of CSIs to flux energy to smaller scales (D'Asaro et al. 2011; Gula et al. 2016; Chor et al. 2022).

The shear production rate can also help distinguish between centrifugal and symmetric modes in CSIs. Namely, centrifugal modes take their energy from the horizontal component of the shears and symmetric modes from the vertical component. Thus, we show only horizontal shear contributions to Π [the sum of $j = 1, 2$ in the rhs of Eq. (17)] in Figs. 13d–f. Comparison with Figs. 13a–c reveals that horizontal shear dominates shear production rates everywhere. Focusing only on active-CSI regions (within dashed lines), the dominance of horizontal shear indicates that CSIs in our domain are largely of centrifugal nature. The possible exception is simulation $\text{Ro}_h = 0.08$ and $S_h = 2.5$ (Figs. 13a,d), where the small part of the domain where CSIs are expected seems to have both vertical and horizontal shear contributions despite the rest of the domain being overwhelmingly dominated by horizontal shear. We note that, in general, it is expected that higher (lower) values of S_h lead to more centrifugal (symmetric) modes in CSIs (Wenegrat et al. 2018, their Fig. 19). However, in our headland configuration, low values of S_h result in terrain-following flows, such that we never get a symmetrically dominated CSI regime in our eddying simulations. It is nonetheless possible that such a regime happens for lower values of the bulk headland slope α .

These results indicate that the CSIs present in our flows tend to be centrifugal in nature. We further note that, given this prevalence of centrifugal modes, the mixing efficiency value of $\gamma \approx 0.2$ we obtain in our simulations (sections 3 and 4) is in line with previous results which indicate that γ is expected to be in the range $\approx 0.2\text{--}0.25$ in such cases (Chor et al. 2022, their Fig. 4). Finally, we again emphasize that, although the geometry chosen in this work includes a vertical wall at the east boundary, that wall has a free-slip boundary condition and therefore does not contribute to produce horizontal

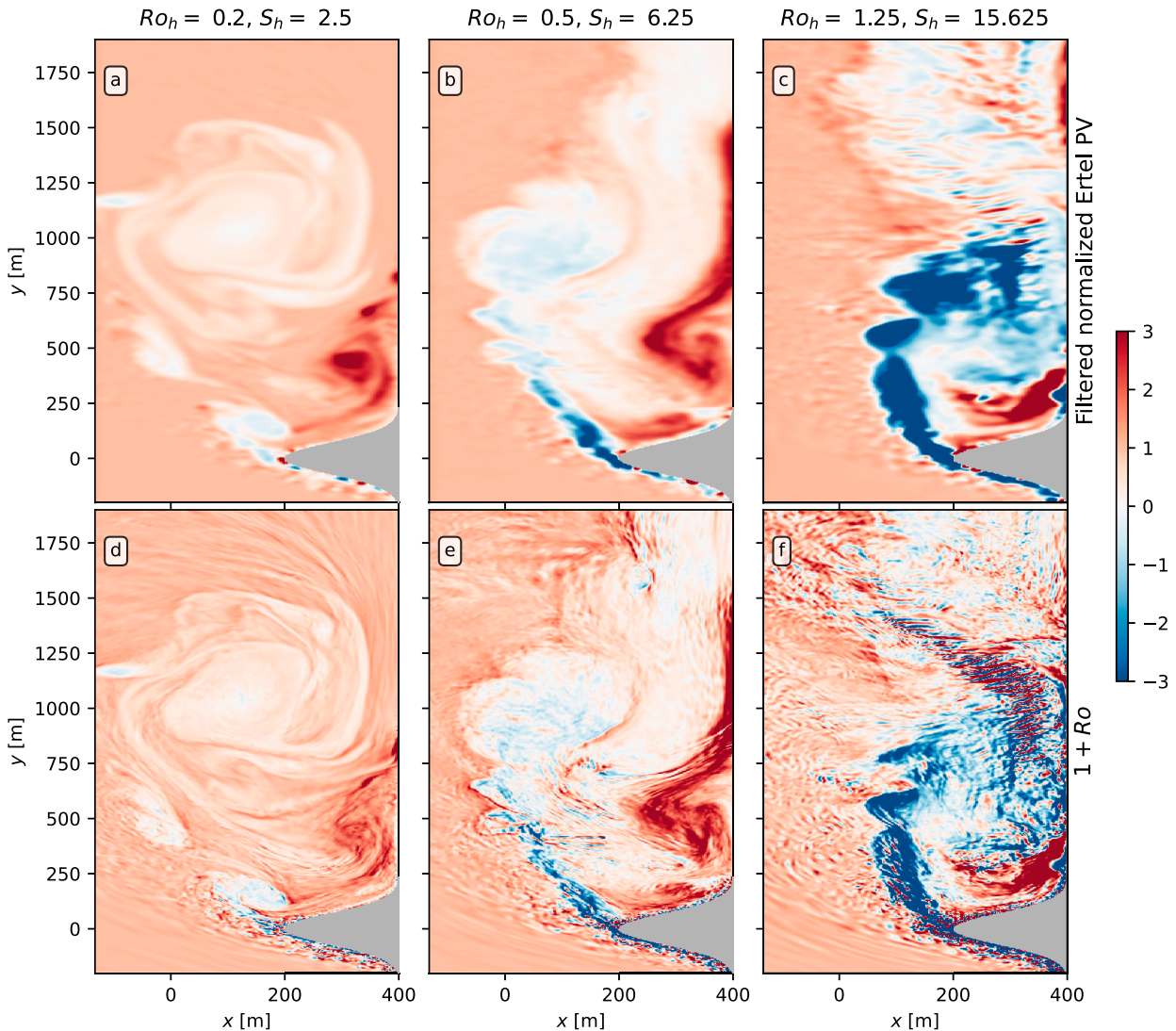


FIG. 12. Comparison between different calculations of Ertel PV at $z \approx 40$ m for snapshots from three simulations with $\text{Fr}_h = 0.08$. (a)–(c) Full (filtered) Ertel PV calculation. (d)–(f) The variable $1 + \text{Ro}$, equivalent to the (unfiltered) vertical component of the full PV.

shear. All the drag in our simulations comes from the headland intrusion, where the slope is $\alpha = 0.2$ —see, for example, Figs. 10a and 10b for an illustration of how the slope remains approximately constant throughout the headland geometry.

6. Discussion and open questions

a. Comparison of energetics with previous RANS results

For context, we can compare our energetic results with those from Gula et al. (2016). We start comparing results in Fig. 8a with their KE budget. The values for the parameters we estimate for their headland at the Great Bahama Bank (see section 3) indicate a headland slope Burger number of $S_h \approx 10$. Approximating the total KE sink due to dissipation in their domain as 0.5 gigawatt (GW) (see their Fig. 5) and using the aforementioned values for V_∞ , L , and H in their simulation, we get a normalized dissipation rate of

$\mathcal{E}_k \approx \mathcal{O}(0.1)$, while the normalized dissipation rate for an equivalent LES according to Fig. 8a is $\mathcal{E}_k \approx \mathcal{O}(1)$. Given that our LESs resolve the small-scale structures whose effect is only parameterized in the hydrostatic simulations of Gula et al. (2016), dissipation results in this manuscript are likely closer to real values. Moreover, it is worth noting that the budget done by Gula et al. (2016) includes at least another two locations of high dissipation in addition to the headland we are considering, making our estimate for their dissipation for a single headland almost certainly an overestimation. Therefore, our results suggest that regional hydrostatic simulations potentially underestimate the dissipation (and, by extension, the mixing) that comes from flow–bathymetry interactions by up to an order of magnitude.

We can also compare the magnitude of ε_k between vertical cross sections in both studies. In our case, a representative value of ε_k based on Fig. 10 is $10^{-9} \text{ W kg}^{-1}$ which,

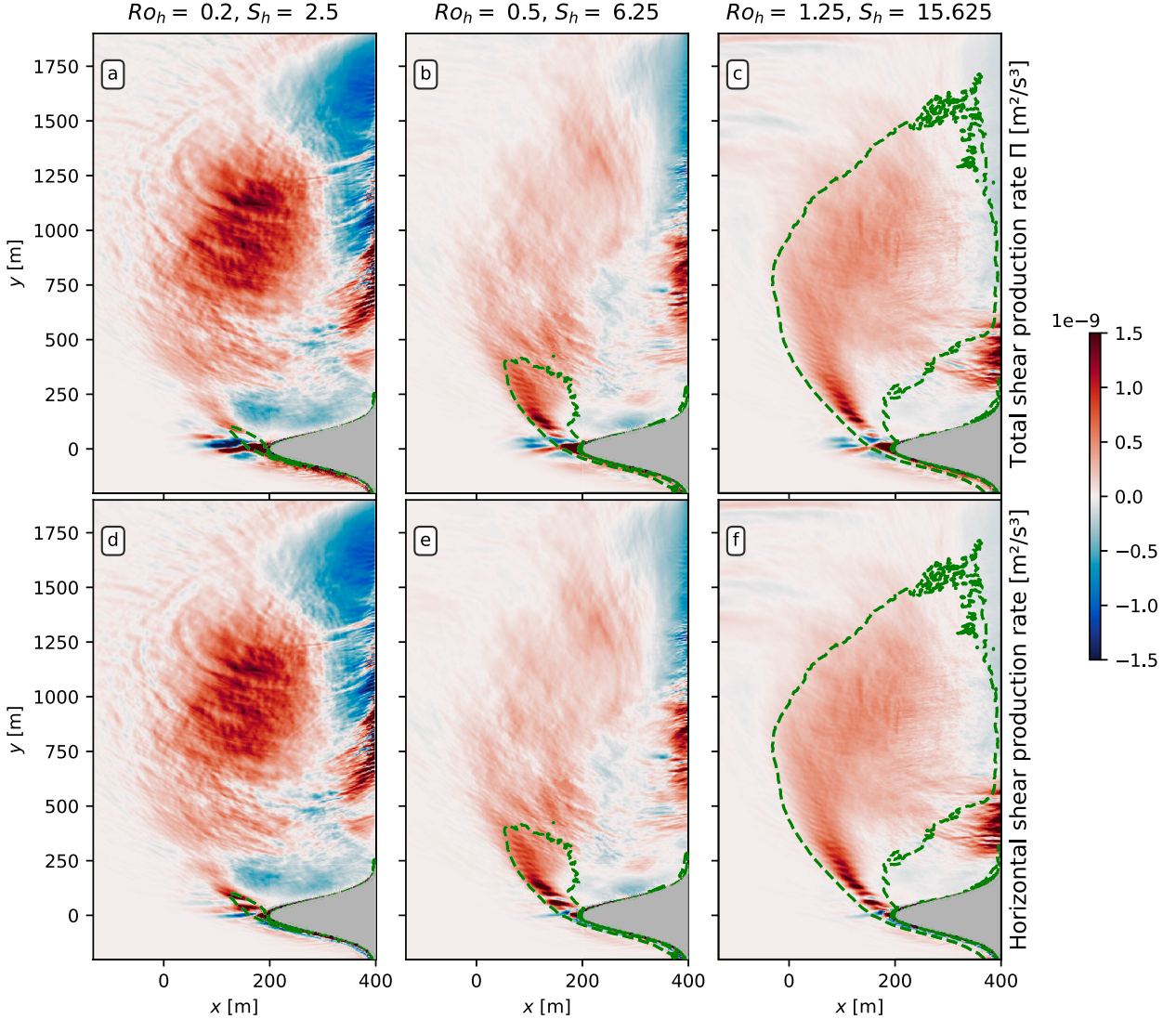


FIG. 13. Horizontal cross sections of shear production rate at $z \approx 40$ m for simulations with $\text{Fr}_h = 0.08$. (a)–(c) Total shear production rates. (d)–(f) Shear production rate due to horizontal shears only. Dashed green lines indicate zero average PV.

normalized, produces $\varepsilon_k/V_\infty^3 L \approx 0.2$. For Gula et al. (2016), a representative value of instantaneous dissipation rate lies between 10^{-6} and $10^{-5} \text{ W kg}^{-1}$, producing values of $\varepsilon_k/V_\infty^3 L$ approximately between 0.005 and 0.05. Consistent with our budget comparison, this result again suggests a potential underestimate of the turbulent dissipation rate due to submeso-scale flow-topography interaction in regional simulations. We further note that a simulation with nondimensional parameters more closely matching those of Gula et al. (2016) (i.e., $\text{Ro}_h = 2$, $\text{Fr}_h = 0.2$, $\alpha = 0.1$) produced very similar figures and dynamics, indicating that these results are robust. However, extra dependencies of \mathcal{E}_k (e.g., on upstream vertical shear or time variability of the incoming flow) may potentially modify dissipation values.

Accordingly, this conclusion indicates that the estimated globally integrated dissipation due to anticyclonic flow-

topography interactions by Gula et al. (2016)—namely, their value of 0.05 terawatts—should be revisited. Revisiting this estimation, however, is not straightforward since, based on Fig. 8a, they used a simulation of the most dissipative regime as a basis for an extrapolation to all ocean bathymetry with a slope higher than ≈ 0.02 . While they account for that fact by noting that the Gulf Stream is highly energetic and lowering their estimated values, that adjustment is at least partly canceled out by their underestimated dissipation, making the final result uncertain. We leave a more precise global estimation (using the trend seen in Fig. 8) for future work, as high-resolution global simulations and bathymetry data would be needed to obtain accurate values of S_h .

The simulations in Gula et al. (2016) used the *K*-profile parameterization (KPP; Large et al. 1994) as a turbulence closure, which uses a simple expression for interior mixing

that is a function of the local gradient Richardson number and two tunable coefficients. Therefore, it is reasonable to expect that, if a RANS simulation using KPP were to correctly reproduce the eddy viscosities seen in our LES, the energetics would likely fall in line with our results. In preliminary investigations, we see a clear organization of viscosity values with Richardson number in an average sense for all simulations in a manner similar to that predicted by KPP. This indicates that a KPP could, in principle, reproduce results in this paper. There are, however, two important caveats. First, we were only able to match KPP's prediction with averaged viscosity values when accounting for the fact that, at coarser resolutions, eddy viscosity values tend to be higher (since stronger gradients are not resolved). Furthermore, while results (after accounting for resolution) were reasonable for the majority of our simulations, a few simulations showed very poor agreement, indicating a dependence on the turbulence physics. This indicates that efforts to improve KPP probably will have to tune coefficients, likely adding resolution dependence and possibly even other dependencies to the expression to account for different physics. Second, while we analyzed these viscosities in an average sense, distribution around these averages may be important, especially considering that dissipation and mixing are emergent phenomena in the flow which are affected by many different feedback mechanisms.

b. CSIs in topographic wakes

We note that, while CSIs have been studied in thermal-wind-balanced flows in nearly all previous investigations (Haine and Marshall 1998; Holton 2004; Thomas and Taylor 2010), the flow in our simulations is mostly ageostrophic and not in thermal wind balance. This is expected to be a generic feature of topographic wakes due to the adverse pressure gradient associated with flow separation. Although work explicitly extending CSI theory beyond thermal wind balance exists, it is focused on expanding on geostrophic balance, rather than not requiring it. Assuming cyclogeostrophic balance as a starting point (i.e., geostrophic balance with an additional curvature term), Buckingham et al. (2021) found that the instability criterion and growth rate are modified by an extra curvature term. With the addition of this curvature term, it is expected that bulk anticyclonic Rossby numbers Ro_b in marginally stable cyclogeostrophic flows be limited to $\text{Ro}_b > -1/2$, which we verified to not be true in our simulations, indicating that curvature effects are not relevant here and our flows are not in cyclogeostrophic balance.

It is possible, however, to derive the criterion for centrifugal instabilities (i.e., CSI in flows without any vertical shear, sometimes called inertial instabilities) without explicitly requiring geostrophic balance. Namely, one can follow the parcel argument by Kloosterziel and van Heijst (1991) and, instead of requiring a pressure gradient force to balance the background flow, simply require a general unspecified force to balance the background state. The only requirement is that such balancing force not be significantly affected by individual parcel displacements. At the end of the derivation, after assuming small curvature effects, one recovers the criterion:

$$f(\zeta + f) < 0, \quad (18)$$

which, assuming $N_\infty^2 > 0$, is equivalent to Eq. (15) for flows without significant vertical shear contributions to PV (which we showed to be true for our simulations in section 5). Thus, this suggests that, at least for the centrifugal modes of CSIs, geostrophic balance is not strictly necessary as long as another force balances the background flow. For the purposes of this work, we posit that this force may be the Reynolds stress divergence (i.e., turbulence), but leave it for future work to investigate this more thoroughly.

Finally, we note that narrow strips of negative PV are very different from the configuration considered in most CSI investigations, which tend to assume a wide environment with negative \hat{q} , such that in general the scale of the counterrotating cells is much smaller than their available space to grow (Haine and Marshall 1998; Taylor and Ferrari 2009; Thomas et al. 2013; Wienkers et al. 2021). In the case of a thin negative PV strip, such as investigated in this section, the scale of the initial cells can overlap with that of the PV strip and possibly even of the secondary Kelvin–Helmholtz instabilities,⁷ which seems to happen in our simulations. In these cases, it is an open problem whether growth rates and other dynamical aspects of CSIs are modified in comparison to more traditional configurations.

7. Conclusions

Due to computational and measurement challenges, the turbulent dynamics of flow–bathymetry interactions are an underexplored topic in physical oceanography. Importantly for this work, there are large uncertainties about how much kinetic energy is dissipated and how much buoyancy is mixed in these locations, with previous work suggesting that the integrated value of these quantities may be significant for global dynamics (Ledwell et al. 2000; Nikurashin and Ferrari 2011; Gula et al. 2016; Zemskova and Grisouard 2021; Evans et al. 2022). Furthermore, there is evidence that these flows generate submesoscale structures (Srinivasan et al. 2019; Perfect et al. 2020b; Srinivasan et al. 2021; Nagai et al. 2021), with unclear implications for flow properties that depend on small-scale turbulence.

Past investigations on the topic largely parameterized the effects of the small scales using RANS models, which do not reliably capture dissipation and mixing rates (Pope 2000). Given the importance of small-scale dynamics to the energy cascade and, consequently, the dissipation and mixing rates in these flows (Chor et al. 2022), we used LES to investigate the aforementioned issues, thus resolving both the submesoscale and turbulent flow structures. We ran a series of simulations where a barotropic, constantly stratified flow interacts with an idealized headland. In these simulations, we systematically change the rotation rate and stratification to reach different

⁷ While for an inviscid fluid the most unstable mode for CSI cells is vanishingly small (Griffiths 2003), the presence of viscosity arrests this process and imposes a finite scale for the fastest growing mode.

parts of the parameter space, spanning four different dynamical regimes. These regimes range from terrain-following flows, where virtually all relevant flow dynamics are concentrated in a relatively thin bottom boundary layer (BBL) attached to the headland, to eddying regimes where most of the interesting dynamics happen at the wake (Figs. 3–6). We found that the slope Burger number S_h is a good predictor of how much turbulence (and hence mixing and dissipation) is concentrated close to the headland, versus downstream from it, with simulations with high S_h being progressively dominated by downstream wake dynamics (Figs. 6 and 7).

In analyzing bulk statistics, we find that the normalized integrated dissipation rate \mathcal{E}_k organizes as

$$\mathcal{E}_k \approx 0.1S_h, \quad (19)$$

and similarly for the normalized integrated buoyancy mixing rate (viz., $\mathcal{E}_p \approx 0.02S_h$). The organization is remarkably robust, especially considering the many pathways for energy transfer that are possible within such a wide range of the parameter space. Although the authors cannot fully explain the dynamical reason for this organization (which is left for future work), it is hypothesized to follow, at least in part, from the form drag, which extracts energy from the barotropic flow at rates that also scale linearly with S_h for most of the parameter space.

It is also worth noting that the organization of \mathcal{E}_k and \mathcal{E}_p persisted in tests where we changed several aspects of the simulations such as V_∞ , boundary conditions, and even bathymetry shape. This gives us confidence in the normalization of KE dissipation and buoyancy mixing rates by V_∞^3/L and allows us to compare our results with those from other simulations on much larger scales. We performed one such comparison with results presented in Gula et al. (2016) for a location in the Gulf Stream, from which we conclude the dynamics of realistic headlands are well captured by our idealized geometry. Additionally, by analyzing both volume-integrated results and snapshots, we conclude that RANS models may underestimate dissipation rates from flow-topography interaction by as much as an order of magnitude. Moreover, we also found that the normalized buoyancy diffusivity \mathcal{K}_b scales as $\mathcal{K}_b \sim \text{Ro}_h \text{Fr}_h$ in our simulations (Fig. 9b). This result is shallower than previous scalings (Perfect et al. 2020a; Mashayek et al. 2024) and suggests a smaller contribution from small-scale topography (which tends to have high Rossby and Froude numbers) to watermass mixing.

We then focused our attention on the regimes that display submesoscale features in the wake, namely, the vertically decoupled eddying, vertically coupled eddying regimes, and the simulations in between them. By repeating the analyses done in section 5 for all simulations, we identify signs of CSIs (which elevate the dissipation rate in comparison to a similar simulation but without CSIs; see section 5 and appendix C) for all simulations in those regimes that have high enough Ro_h (therefore reaching sufficiently negative Ro values in the wake to have a negative PV signal). Although CSIs in our domain derive their energy mostly from horizontal shear production (being similar to centrifugal instabilities), they exist in

an ageostrophic flow and, as such, differ from the traditional picture of CSIs as emerging in thermal-wind-balanced flow (Haine and Marshall 1998).

Furthermore, while theory and measurements in the upper ocean indicate that submesoscales modify energetics when compared to more traditional upper-ocean turbulence (Thomas and Taylor 2010; Taylor and Ferrari 2010; D'Asaro et al. 2011; Thomas et al. 2013, 2016), the excellent organization of dissipation and mixing with S_h across different regimes (some with and others without CSIs) suggests otherwise for topographic wakes. Thus, while the route to turbulence seems to be important in setting the energetics of upper-ocean flows, our results in Figs. 8a and 9a suggest that, given a barotropic flow and an obstacle in the ocean bottom, the small-scale dynamics adjust following a general principle. One important difference between our configuration and upper-ocean CSI is that, despite the controlling role of surface fluxes, the latter sources their energy from the balanced upper-ocean flow (e.g., Taylor and Ferrari 2010). In our simulations, despite the route to turbulence changing from one regime to the other, the energy source is always in some sense initially set by the balanced inflow interacting with the topography, hence the cross-regime organization of results. Another possible explanation for this difference in energetics behavior between upper-ocean CSI and bottom CSIs is their type and the characteristics of the background flow. Namely, CSI studies in the upper ocean have mostly investigated symmetrically dominated CSIs (symmetric instabilities) in a flow that is approximately in thermal wind balance. For CSIs in our headland wakes, the modes are mostly centrifugal, and the flow is ageostrophic.

Finally, we opted for an idealized headland as the geometry of choice for our investigation given the size limitations of the LES technique. While we are aware that such a shape cannot possibly capture the detailed dynamics that emerge when real ocean flows interact with complex, real bathymetry, we hope that many of the high-level physics carry over to realistic scenarios. This seems to be true given our comparison with simulations from Gula et al. (2016) and with preliminary LES using different bathymetry shapes, and there are ongoing efforts by the authors to verify this hypothesis more completely in future work.

Acknowledgments. T. C. and J. O. W. were supported by the National Science Foundation Grants OCE-1948953 and OCE-2242182 (T. C. and J. O. W.), and Office of Naval Research Grant N000142412583 (J. O. W.) is gratefully acknowledged. We are thankful to Dr. Leif Thomas for insightful feedback, as well as Dr. Kaushik Srinivasan and an anonymous reviewer for their helpful comments. We would also like to acknowledge high-performance computing support from Cheyenne (<https://doi.org/10.5065/qx9a-pg09>) provided by NCAR's Computational and Information Systems Laboratory, sponsored by the National Science Foundation.

Data availability statement. The numerical model simulations upon which this study is based are too large to easily

archive or transfer. Instead, all the code used to generate the results is available at <https://doi.org/10.5281/zenodo.1427667> (Chor 2024).

APPENDIX A

Grid Resolution Analysis

[Khani \(2018\)](#) compared LES of idealized stratified turbulent flows against direct numerical simulations and found that LES produced correct results when their grid spacing was approximately equal to or smaller than the Ozmidov length scale ([Khani and Waite 2014; Khani 2018](#)):

$$L_O = 2\pi \left(\langle \overline{\varepsilon_k} \rangle^e \right)^{1/2} / N_0^3, \quad (\text{A1})$$

where $\langle \overline{\varepsilon_k} \rangle^e$ is a time and volume average of ε_k over turbulent regions of the flow (which we implement here as an average over regions where $\varepsilon_k > 10^{-10} \text{ m}^2 \text{ s}^{-3}$). Thus, we compare our grid spacing with the Ozmidov length, plotting the quantity $\Delta z/L_O$ as a function of S_h in Fig. A1 for all points in the parameter space used in this work. Note that, to also illustrate convergence, we ran extra simulations that are exactly the same as the ones whose results are presented in the main text, except for the spacings Δx , Δy , and Δz , which were increased by factors of 2 while keeping the ratios $\Delta x/\Delta z = \Delta y/\Delta z$ constant. It is clear that there is general trend for simulations with lower S_h to be more well resolved, owing primarily to the lower stratification, with simulations being better resolved with decreasing Δz , as expected. It is also clear that all the simulations used to produce the results in this paper (black points) meet or exceed the threshold identified by [Khani \(2018\)](#) and therefore can be considered converged. Moreover, we note that even with the half-resolution simulations ($\Delta z \approx 1.2 \text{ m}$; gray points), all results in this work remain qualitatively

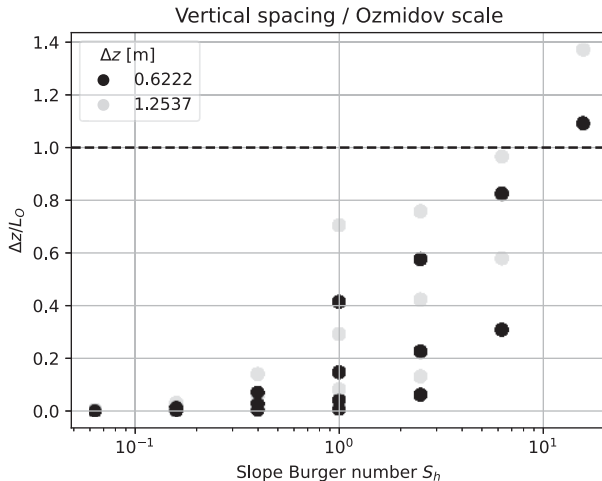


FIG. A1. The $\Delta z/L_O$ as a function of S_h . Results presented in this work are obtained with $\Delta z \approx 0.6 \text{ m}$ (black points). The dashed black line shows $\Delta z/L_0 = 1$, for reference.

the same, with only minor quantitative differences, further indicating that our simulations are well converged.

APPENDIX B

Bulk Results for Cyclonic Configuration

In this appendix, we analyze bulk energetic results for the cyclonic configuration (i.e., the same simulations as depicted in Fig. 2 but with a negative-sign Coriolis frequency) in comparison with their anticyclonic counterparts. We start with the normalized integrated KE dissipation rate \mathcal{E}_k , which is shown in Fig. B1a for the anticyclonic (blue diamonds) and cyclonic (red crosses) simulations. In accordance with the comparison made in section 5, we see that, in general, cyclonic simulations tend to have lower KE dissipation rates. We also see an organization of results into a scaling close to $\sim S_h^{1/2}$ (red dashed line), shallower than the relationship observed for the anticyclonic results of S_h (blue dashed line). In Fig. B1b, we show results for the normalized integrated buoyancy mixing rate \mathcal{E}_p for both configurations. Similarly to the dissipation results, buoyancy mixing rates seem to organize in a shallower scaling of $S_h^{1/2}$ for the cyclonic simulations. With the exception of simulations with $S_h < 0.2$, \mathcal{E}_p values also seem to be lower for cyclonic simulations, in comparison with anticyclonic ones.

Thus, while dissipation and mixing rates seem to also follow a general principle for cyclonic headland flows, they exhibit a shallower scaling with S_h and tend to dissipate and

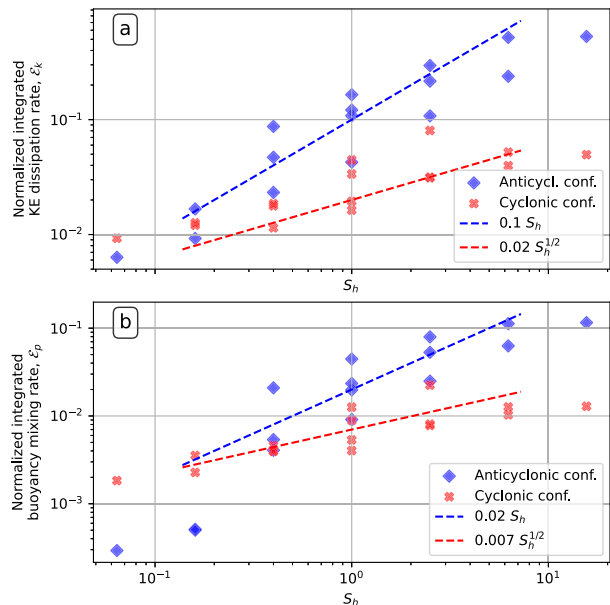


FIG. B1. Normalized volume-integrated, time-averaged quantities as a function of slope Burger number S_h . (a) KE dissipation rates. (b) Buoyancy mixing rates. Blue diamonds are results for the anticyclonic simulations (same data as plotted in Figs. 8a,b) and red diamonds are results for the cyclonic simulations, which have the exact same configuration as the anticyclonic ones, but with opposite-sign Coriolis frequency.

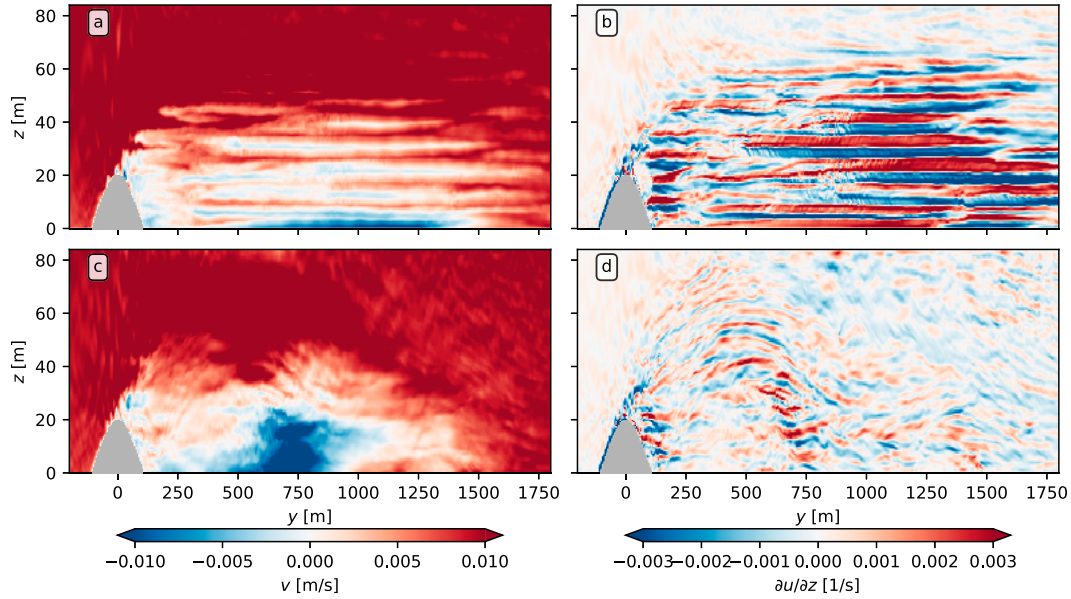


FIG. B2. Vertical cross sections of simulation with $\text{Ro}_h = 1.25$, $\text{Fr}_h = 0.08$, and $S_h \approx 15.6$ in an (top) anticyclonic and (bottom) cyclonic headland interaction. (a),(c) Streamwise velocity and (b),(d) u -direction vertical shear. While the anticyclonic flow is vertically decoupled, resulting in high levels of vertical shear, the cyclonic flow remains vertically coherent after detachment, with significantly lower levels of vertical shear.

mix less than their anticyclonic counterparts, with the difference being larger for higher values of S_h . Note that the fact that cyclonic headlands also exhibit a consistent scaling across regimes is in line with our hypothesis that such an organization comes from the flow having the same source of energy in all simulations. Namely, the energy source is always initially set by the balanced inflow interacting with the topography (see section 7).

However, the fact that the discrepancy between cyclonic and anticyclonic headland encounters is larger for larger S_h differs from results by Srinivasan et al. (2021) for seamounts. Namely, Srinivasan et al. (2021) observed that, due to the increasing predominance of vertical shear as a mixing mechanism as rotation is decreased, flows with higher Rossby number (and thus higher S_h) dissipate KE at similar rates in both cyclonic and anticyclonic seamount wake eddies. In short, findings from seamount simulations imply that the higher the Rossby and slope Burger numbers, the more symmetric the energetics should be between cyclonic and anticyclonic, which, as Fig. B1 shows, does not happen in headlands.

This discrepancy can be explained by the fact that, while high slope Burger numbers correlate with vertically decoupled flows in both anticyclonic headland interactions and seamounts, this is not true of cyclonic headlands. We illustrate this in Fig. B2 with simulation $\text{Ro}_h = 1$ and $\text{Fr}_h = 0.08$, which is our simulation with the highest S_h and largest discrepancy between cyclonic and anticyclonic flow dissipations. It is clear from the figure that cyclonic flows remain vertically coherent after detachment, even as their anticyclonic counterparts decouple vertically (Figs. B2a,c). This translates into significantly lower vertical shear rates for cyclonic headland interactions

(Figs. B2b,d). The different scaling seen in cyclonic headlands is qualitatively in agreement with this fact, given that it suggests that the important underlying processes are different between the cyclonic and anticyclonic cases. This further suggests that, in seamounts, it may be the anticyclonic side of the wake that causes vertical decoupling of lee eddies. Given the focus of this manuscript on anticyclonic headland wakes, we leave further investigation of this phenomenon for future studies.

APPENDIX C

Centrifugal-Symmetric Instabilities in Vertically Coupled Eddying Simulation

For a more complete picture of the parameter space and to compare with results presented in section 5, we show snapshots of normalized Ertel PV, KE dissipation rates, and streamwise vorticity for a simulation in the vertically coupled eddying regime and its cyclonic counterpart. Results for the anticyclonic vertically coupled headland are presented in Fig. C1, where one can see an evolution that is similar to the vertically decoupled regime (Fig. 10). Namely, there are overturning circulations that coincide with patches of negative PV as well as high KE dissipation rates (particularly visible at 80 m; panels a, d, and g). As the flow progresses downstream, the negative PV signal is mixed away and the dissipation rates accordingly decrease. The main difference between the results in Figs. C1 and 10 is that the simulation in the vertically coupled eddying regime has a weaker negative PV signal since it has a higher Coriolis frequency f and therefore generates a Ro signal that is smaller in magnitude. As a result, the CSIs

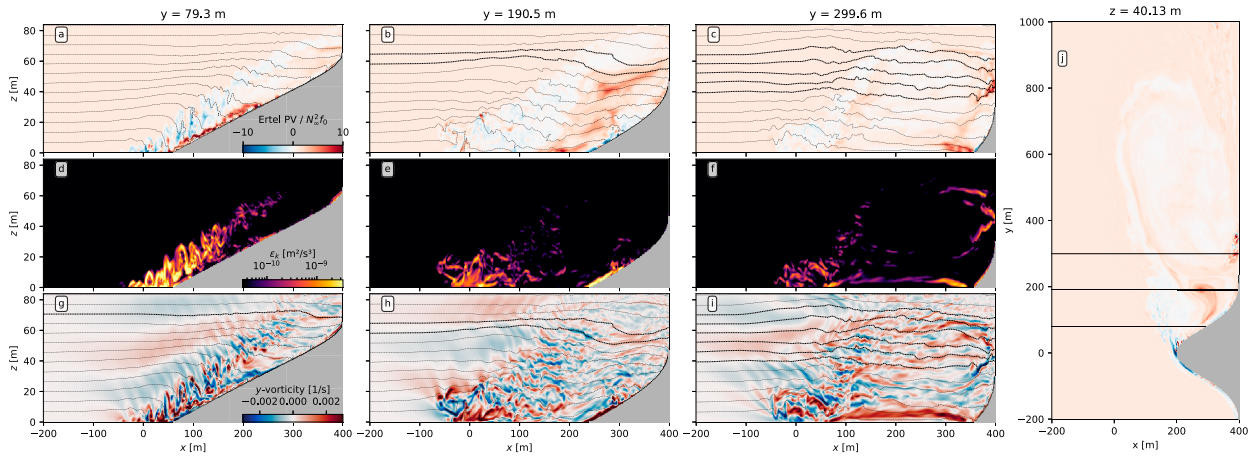


FIG. C1. As in Fig. 10, but for simulation with $\text{Ro}_h = \text{Fr}_h = 0.2$.

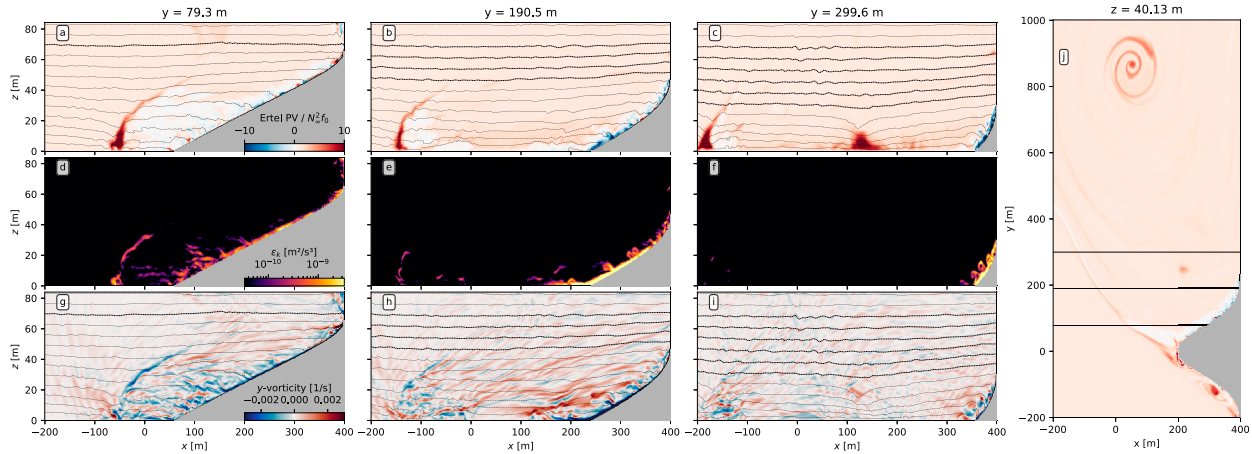


FIG. C2. As in Fig. 10, but for simulation with $\text{Ro}_h = \text{Fr}_h = 0.2$ and with opposite sign f .

are able to mix away that negative PV signal faster, despite having a slower growth rate (this can also be seen in Fig. C1j).

Figure C2 shows a similar progression but for a cyclonic headland in a vertically coupled eddying regime. As is the case with the simulations in the vertically decoupled eddying regime, the cyclonic interaction has much lower dissipation rates since the flow produces mainly cyclonic PV and as a result is therefore mostly stable to CSIs. The small portion of the domain that has a negative normalized PV signal (viz., the return flow very close to the headland) does have elevated dissipation and has overturning motions typical of CSI activity.

REFERENCES

- Adcroft, A., C. Hill, and J. Marshall, 1997: Representation of topography by shaved cells in a height coordinate ocean model. *Mon. Wea. Rev.*, **125**, 2293–2315, [https://doi.org/10.1175/1520-0493\(1997\)125<2293:ROTBC>2.0.CO;2](https://doi.org/10.1175/1520-0493(1997)125<2293:ROTBC>2.0.CO;2).
- Armi, L., 1978: Some evidence for boundary mixing in the deep ocean. *J. Geophys. Res.*, **83**, 1971–1979, <https://doi.org/10.1029/JC083iC04p01971>.
- Bachman, S. D., B. Fox-Kemper, J. R. Taylor, and L. N. Thomas, 2017: Parameterization of frontal symmetric instabilities. I: Theory for resolved fronts. *Ocean Modell.*, **109**, 72–95, <https://doi.org/10.1016/j.ocemod.2016.12.003>.
- Bastos, A., M. Collins, and N. Kenyon, 2003: Water and sediment movement around a coastal headland: Portland bill, southern UK. *Ocean Dyn.*, **53**, 309–321, <https://doi.org/10.1007/s10236-003-0031-1>.
- Belcher, S. E., and J. C. R. Hunt, 1998: Turbulent flow over hills and waves. *Annu. Rev. Fluid Mech.*, **30**, 507–538, <https://doi.org/10.1146/annurev.fluid.30.1.507>.
- Ben Hamza, S., S. Habli, N. Mahjoub Saïd, H. Bournot, and G. Le Palec, 2015: Simulation of pollutant dispersion of a free surface flow in coastal water. *Ocean Eng.*, **108**, 81–97, <https://doi.org/10.1016/j.oceaneng.2015.07.059>.
- Bodner, A. S., and B. Fox-Kemper, 2020: A breakdown in potential vorticity estimation delineates the submesoscale-to-turbulence boundary in large eddy simulations. *J. Adv. Model. Earth Syst.*, **12**, e2020MS002049, <https://doi.org/10.1029/2020MS002049>.
- Brearley, J. A., K. L. Sheen, A. C. N. Garabato, D. A. Smed, and S. Waterman, 2013: Eddy-induced modulation of turbulent dissipation over rough topography in the Southern Ocean.

- J. Phys. Oceanogr.*, **43**, 2288–2308, <https://doi.org/10.1175/JPO-D-12-0222.1>.
- Buckingham, C. E., J. Gula, and X. Carton, 2021: The role of curvature in modifying frontal instabilities. Part I: Review of theory and presentation of a nondimensional instability criterion. *J. Phys. Oceanogr.*, **51**, 299–315, <https://doi.org/10.1175/JPO-D-19-0265.1>.
- Capó, E., J. C. McWilliams, and A. Jagannathan, 2023: Flow-topography interaction along the Spanish slope in the Alboran Sea: Vorticity generation and connection to interior fronts. *J. Geophys. Res. Oceans*, **128**, e2022JC019480, <https://doi.org/10.1029/2022JC019480>.
- Caulfield, C. P., 2021: Layering, instabilities, and mixing in turbulent stratified flows. *Annu. Rev. Fluid Mech.*, **53**, 113–145, <https://doi.org/10.1146/annurev-fluid-042320-100458>.
- Chamecki, M., T. Chor, D. Yang, and C. Meneveau, 2019: Material transport in the ocean mixed layer: Recent developments enabled by large eddy simulations. *Rev. Geophys.*, **57**, 1338–1371, <https://doi.org/10.1029/2019RG000655>.
- Chen, G., and Coauthors, 2015: Observed deep energetic eddies by seamount wake. *Sci. Rep.*, **5**, 17416, <https://doi.org/10.1038/srep17416>.
- Chor, T., 2024: Code for the paper “The turbulent dynamics of anticyclonic submesoscale headland wakes”. Zenodo, <https://doi.org/10.5281/zenodo.14276676>.
- , J. C. McWilliams, and M. Chamecki, 2021: Modifications to the K -profile parameterization with nondiffusive fluxes for Langmuir turbulence. *J. Phys. Oceanogr.*, **51**, 1503–1521, <https://doi.org/10.1175/JPO-D-20-0250.1>.
- , J. O. Wenegrat, and J. Taylor, 2022: Insights into the mixing efficiency of submesoscale centrifugal-symmetric instabilities. *J. Phys. Oceanogr.*, **52**, 2273–2287, <https://doi.org/10.1175/JPO-D-21-0259.1>.
- D’Asaro, E., C. Lee, L. Rainville, R. Harcourt, and L. Thomas, 2011: Enhanced turbulence and energy dissipation at ocean fronts. *Science*, **332**, 318–322, <https://doi.org/10.1126/science.1201515>.
- de Lavergne, C., G. Madec, J. Le Sommer, A. J. G. Nurser, and A. C. Naveira Garabato, 2016: On the consumption of Antarctic bottom water in the abyssal ocean. *J. Phys. Oceanogr.*, **46**, 635–661, <https://doi.org/10.1175/JPO-D-14-0201.1>.
- Dewar, W. K., J. C. McWilliams, and M. J. Molemaker, 2015: Centrifugal instability and mixing in the California undercurrent. *J. Phys. Oceanogr.*, **45**, 1224–1241, <https://doi.org/10.1175/JPO-D-13-0269.1>.
- Ding, G.-Y., Y.-H. He, and K.-Q. Xia, 2022: The effect of tidal force and topography on horizontal convection. *J. Fluid Mech.*, **932**, A38, <https://doi.org/10.1017/jfm.2021.1026>.
- Edwards, K. A., P. MacCready, J. N. Moum, G. Pawlak, J. M. Klymak, and A. Perlin, 2004: Form drag and mixing due to tidal flow past a sharp point. *J. Phys. Oceanogr.*, **34**, 1297–1312, [https://doi.org/10.1175/1520-0485\(2004\)034<1297:FDAMDT>2.0.CO;2](https://doi.org/10.1175/1520-0485(2004)034<1297:FDAMDT>2.0.CO;2).
- Evans, D. G., E. Frajka-Williams, and A. C. Naveira Garabato, 2022: Dissipation of mesoscale eddies at a western boundary via a direct energy cascade. *Sci. Rep.*, **12**, 887, <https://doi.org/10.1038/s41598-022-05002-7>.
- Ferrari, R., and C. Wunsch, 2009: Ocean circulation kinetic energy: Reservoirs, sources, and sinks. *Annu. Rev. Fluid Mech.*, **41**, 253–282, <https://doi.org/10.1146/annurev.fluid.40.111406.102139>.
- , A. Mashayek, T. J. McDougall, M. Nikurashin, and J.-M. Campin, 2016: Turning ocean mixing upside down. *J. Phys. Oceanogr.*, **46**, 2239–2261, <https://doi.org/10.1175/JPO-D-15-0244.1>.
- Finnigan, J., and Coauthors, 2020: Boundary-layer flow over complex topography. *Bound.-Layer Meteor.*, **177**, 247–313, <https://doi.org/10.1007/s10546-020-00564-3>.
- Gill, A., 1982: *Atmosphere-Ocean Dynamics*. International Geophysics Series, Vol. 30, Academic Press, 662 pp.
- Gregg, M. C., E. A. D’Asaro, J. J. Riley, and E. Kunze, 2018: Mixing efficiency in the ocean. *Ann. Rev. Mar. Sci.*, **10**, 443–473, <https://doi.org/10.1146/annurev-marine-121916-063643>.
- Griffiths, S. D., 2003: Nonlinear vertical scale selection in equatorial inertial instability. *J. Atmos. Sci.*, **60**, 977–990, [https://doi.org/10.1175/1520-0469\(2003\)060<0977:NVSSIE>2.0.CO;2](https://doi.org/10.1175/1520-0469(2003)060<0977:NVSSIE>2.0.CO;2).
- Gula, J., M. J. Molemaker, and J. C. McWilliams, 2016: Topographic generation of submesoscale centrifugal instability and energy dissipation. *Nat. Commun.*, **7**, 12811, <https://doi.org/10.1038/ncomms12811>.
- Haine, T. W. N., and J. Marshall, 1998: Gravitational, symmetric, and baroclinic instability of the ocean mixed layer. *J. Phys. Oceanogr.*, **28**, 634–658, [https://doi.org/10.1175/1520-0485\(1998\)028<0634:GSABIO>2.0.CO;2](https://doi.org/10.1175/1520-0485(1998)028<0634:GSABIO>2.0.CO;2).
- Holton, J. R., 2004: *An Introduction to Dynamic Meteorology*. 4th ed. Academic Press, 535 pp.
- Jalali, M., and S. Sarkar, 2017: Large eddy simulation of flow and turbulence at the steep topography of Luzon strait. *Geophys. Res. Lett.*, **44**, 9440–9448, <https://doi.org/10.1002/2017GL074119>.
- Johnston, T. M. S., and Coauthors, 2019: Fleat: A multiscale observational and modeling program to understand how topography affects flows in the western North Pacific. *Oceanography*, **32** (4), 10–21, <https://doi.org/10.5670/oceanog.2019.407>.
- Khani, S., 2018: Mixing efficiency in large-eddy simulations of stratified turbulence. *J. Fluid Mech.*, **849**, 373–394, <https://doi.org/10.1017/jfm.2018.417>.
- , and M. L. Waite, 2014: Buoyancy scale effects in large-eddy simulations of stratified turbulence. *J. Fluid Mech.*, **754**, 75–97, <https://doi.org/10.1017/jfm.2014.381>.
- Kim, S.-S., and P. Wessel, 2011: New global seamount census from altimetry-derived gravity data. *Geophys. J. Int.*, **186**, 615–631, <https://doi.org/10.1111/j.1365-246X.2011.05076.x>.
- Kleissl, J., V. Kumar, C. Meneveau, and M. B. Parlange, 2006: Numerical study of dynamic Smagorinsky models in large-eddy simulation of the atmospheric boundary layer: Validation in stable and unstable conditions. *Water Resour. Res.*, **42**, W06D10, <https://doi.org/10.1029/2005WR004685>.
- Kloosterziel, R. C., and G. J. F. van Heijst, 1991: An experimental study of unstable barotropic vortices in a rotating fluid. *J. Fluid Mech.*, **223**, 1–24, <https://doi.org/10.1017/S0022112091001301>.
- Klymak, J. M., 2018: Nonpropagating form drag and turbulence due to stratified flow over large-scale abyssal hill topography. *J. Phys. Oceanogr.*, **48**, 2383–2395, <https://doi.org/10.1175/JPO-D-17-0225.1>.
- , D. Balwada, A. N. Garabato, and R. Abernathey, 2021: Parameterizing nonpropagating form drag over rough bathymetry. *J. Phys. Oceanogr.*, **51**, 1489–1501, <https://doi.org/10.1175/JPO-D-20-0112.1>.
- Large, W. G., J. C. McWilliams, and S. C. Doney, 1994: Oceanic vertical mixing: A review and a model with a nonlocal boundary layer parameterization. *Rev. Geophys.*, **32**, 363–403, <https://doi.org/10.1029/94RG01872>.
- Ledwell, J. R., E. T. Montgomery, K. L. Polzin, L. C. St. Laurent, R. W. Schmitt, and J. M. Toole, 2000: Evidence for enhanced mixing over rough topography in the abyssal ocean. *Nature*, **403**, 179–182, <https://doi.org/10.1038/35003164>.

- Lentz, S. J., and D. C. Chapman, 2004: The importance of non-linear cross-shelf momentum flux during wind-driven coastal upwelling. *J. Phys. Oceanogr.*, **34**, 2444–2457, <https://doi.org/10.1175/JPO2644.1>.
- Lilly, D. K., 1962: On the numerical simulation of buoyant convection. *Tellus*, **14A**, 148–172, <https://doi.org/10.1111/j.2153-3490.1962.tb00128.x>.
- MacCready, P., and P. B. Rhines, 1991: Buoyant inhibition of Ekman transport on a slope and its effect on stratified spin-up. *J. Fluid Mech.*, **223**, 631–661, <https://doi.org/10.1017/S0022112091001581>.
- , G. Pawlak, K. Edwards, and R. McCabe, 2003: Form drag on ocean flows. *Near Boundary Processes and their Parameterization: Proc. ‘Aha Huliko’a Hawaiian Winter Workshop*, Honolulu, HI, University of Hawai‘i at Mōnoa, 119–130, <https://api.semanticscholar.org/CorpusID:2118755>.
- MacKinnon, J. A., and Coauthors, 2017: Climate process team on internal wave–driven ocean mixing. *Bull. Amer. Meteor. Soc.*, **98**, 2429–2454, <https://doi.org/10.1175/BAMS-D-16-0030.1>.
- Magaldi, M. G., T. M. Özgökmen, A. Griffa, E. P. Chassignet, M. Iskandarani, and H. Peters, 2008: Turbulent flow regimes behind a coastal cape in a stratified and rotating environment. *Ocean Modell.*, **25**, 65–82, <https://doi.org/10.1016/j.ocemod.2008.06.006>.
- Mashayek, A., 2023: Large-scale impacts of small-scale ocean topography. *J. Fluid Mech.*, **964**, F1, <https://doi.org/10.1017/jfm.2023.305>.
- , J. Gula, L. E. Baker, A. C. Naveira Garabato, L. Cimoli, J. J. Riley, and C. de Lavergne, 2024: On the role of seamounts in upwelling deep-ocean waters through turbulent mixing. *Proc. Natl. Acad. Sci. USA*, **121**, e2322163121, <https://doi.org/10.1073/pnas.2322163121>.
- McCabe, R. M., P. MacCready, and G. Pawlak, 2006: Form drag due to flow separation at a headland. *J. Phys. Oceanogr.*, **36**, 2136–2152, <https://doi.org/10.1175/JPO2966.1>.
- McDougall, T. J., and R. Ferrari, 2017: Abyssal upwelling and downwelling driven by near-boundary mixing. *J. Phys. Oceanogr.*, **47**, 261–283, <https://doi.org/10.1175/JPO-D-16-0082.1>.
- McWilliams, J. C., 2016: Submesoscale currents in the ocean. *Proc. Roy. Soc.*, **472A**, 20160117, <https://doi.org/10.1098/rspa.2016.0117>.
- Melet, A., M. Nikurashin, C. Muller, S. Falahat, J. Nylander, P. G. Timko, B. K. Arbic, and J. A. Goff, 2013: Internal tide generation by abyssal hills using analytical theory. *J. Geophys. Res. Oceans*, **118**, 6303–6318, <https://doi.org/10.1002/2013JC009212>.
- Molemaker, M. J., J. C. McWilliams, and W. K. Dewar, 2015: Submesoscale instability and generation of mesoscale anticyclones near a separation of the California undercurrent. *J. Phys. Oceanogr.*, **45**, 613–629, <https://doi.org/10.1175/JPO-D-13-0225.1>.
- Munk, W., and C. Wunsch, 1998: Abyssal recipes II: Energetics of tidal and wind mixing. *Deep-Sea Res. I*, **45**, 1977–2010, [https://doi.org/10.1016/S0967-0637\(98\)00070-3](https://doi.org/10.1016/S0967-0637(98)00070-3).
- Nagai, T., and Coauthors, 2021: The Kuroshio flowing over seamounts and associated submesoscale flows drive 100-km-wide 100–1000-fold enhancement of turbulence. *Commun. Earth Environ.*, **2**, 170, <https://doi.org/10.1038/s43247-021-00230-7>.
- Nencioli, F., F. d’Ovidio, A. M. Doglioli, and A. A. Petrenko, 2011: Surface coastal circulation patterns by in-situ detection of Lagrangian coherent structures. *Geophys. Res. Lett.*, **38**, L17604, <https://doi.org/10.1029/2011GL048815>.
- Nikurashin, M., and R. Ferrari, 2011: Global energy conversion rate from geostrophic flows into internal lee waves in the deep ocean. *Geophys. Res. Lett.*, **38**, L08610, <https://doi.org/10.1029/2011GL046576>.
- Pedlosky, J., 1987: *Geophysical Fluid Dynamics*. 2nd ed. Springer, 710 pp.
- Peltier, W. R., and C. P. Caulfield, 2003: Mixing efficiency in stratified shear flows. *Annu. Rev. Fluid Mech.*, **35**, 135–167, <https://doi.org/10.1146/annurev.fluid.35.101101.161144>.
- Perfect, B., N. Kumar, and J. J. Riley, 2018: Vortex structures in the wake of an idealized seamount in rotating, stratified flow. *Geophys. Res. Lett.*, **45**, 9098–9105, <https://doi.org/10.1029/2018GL078703>.
- , —, and —, 2020a: Energetics of seamount wakes. Part I: Energy exchange. *J. Phys. Oceanogr.*, **50**, 1365–1382, <https://doi.org/10.1175/JPO-D-19-0105.1>.
- , —, and —, 2020b: Energetics of seamount wakes. Part II: Wave fluxes. *J. Phys. Oceanogr.*, **50**, 1383–1398, <https://doi.org/10.1175/JPO-D-19-0104.1>.
- Polzin, K. L., and T. J. McDougall, 2022: Mixing at the ocean’s bottom boundary. *Ocean Mixing*, M. Meredith and A. Naveira Garabato, Eds., Elsevier, 145–180, <https://doi.org/10.1016/B978-0-12-821512-8.00014-1>.
- , J. M. Toole, J. R. Ledwell, and R. W. Schmitt, 1997: Spatial variability of turbulent mixing in the abyssal ocean. *Science*, **276**, 93–96, <https://doi.org/10.1126/science.276.5309.93>.
- Pope, S. B., 2000: *Turbulent Flows*. Cambridge University Press, 771 pp., <https://doi.org/10.1017/CBO9780511840531>.
- Puthan, P., M. Jalali, J. L. Ortiz-Tarin, K. Chongsiripinyo, G. Pawlak, and S. Sarkar, 2020: The wake of a three-dimensional underwater obstacle: Effect of bottom boundary conditions. *Ocean Modell.*, **149**, 101611, <https://doi.org/10.1016/j.ocemod.2020.101611>.
- Radko, T., 2023: A generalized theory of flow forcing by rough topography. *J. Fluid Mech.*, **961**, A24, <https://doi.org/10.1017/jfm.2023.169>.
- Ramadhan, A., and Coauthors, 2020: Oceananigans.jl: Fast and friendly geophysical fluid dynamics on GPUs. *J. Source Software*, **5**, 2018, <https://doi.org/10.21105/joss.02018>.
- Rozema, W., H. J. Bae, P. Moin, and R. Verstappen, 2015: Minimum-dissipation models for large-eddy simulation. *Phys. Fluids*, **27**, 085107, <https://doi.org/10.1063/1.4928700>.
- Scott, R. B., J. A. Goff, A. C. Naveira Garabato, and A. J. G. Nurser, 2011: Global rate and spectral characteristics of internal gravity wave generation by geostrophic flow over topography. *J. Geophys. Res.*, **116**, C09029, <https://doi.org/10.1029/2011JC007005>.
- Shchepetkin, A. F., and J. C. McWilliams, 2005: The regional oceanic modeling system (ROMS): A split-explicit, free-surface, topography-following-coordinate oceanic model. *Ocean Modell.*, **9**, 347–404, <https://doi.org/10.1016/j.ocemod.2004.08.002>.
- Smagorinsky, J., 1963: General circulation experiments with the primitive equations: I. The basic experiment. *Mon. Wea. Rev.*, **91**, 99–164, [https://doi.org/10.1175/1520-0493\(1963\)091<099:GCEWTP>2.3.CO;2](https://doi.org/10.1175/1520-0493(1963)091<099:GCEWTP>2.3.CO;2).
- Spingys, C. P., A. C. Naveira Garabato, S. Legg, K. L. Polzin, E. P. Abrahamsen, C. E. Buckingham, A. Forryan, and E. E. Frajka-Williams, 2021: Mixing and transformation in a deep western boundary current: A case study. *J. Phys. Oceanogr.*, **51**, 1205–1222, <https://doi.org/10.1175/JPO-D-20-0132.1>.
- Srinivasan, K., J. C. McWilliams, M. J. Molemaker, and R. Barkan, 2019: Submesoscale vortical wakes in the lee of topography.

- J. Phys. Oceanogr.*, **49**, 1949–1971, <https://doi.org/10.1175/JPO-D-18-0042.1>.
- , —, and A. Jagannathan, 2021: High vertical shear and dissipation in equatorial topographic wakes. *J. Phys. Oceanogr.*, **51**, 1985–2001, <https://doi.org/10.1175/JPO-D-20-0119.1>.
- St John, M. A., and S. Pond, 1992: Tidal plume generation around a promontory: Effects on nutrient concentrations and primary productivity. *Cont. Shelf Res.*, **12**, 339–354, [https://doi.org/10.1016/0278-4343\(92\)90035-I](https://doi.org/10.1016/0278-4343(92)90035-I).
- Taylor, J. R., and R. Ferrari, 2009: On the equilibration of a symmetrically unstable front via a secondary shear instability. *J. Fluid Mech.*, **622**, 103–113, <https://doi.org/10.1017/S0022112008005272>.
- , —, 2010: Buoyancy and wind-driven convection at mixed layer density fronts. *J. Phys. Oceanogr.*, **40**, 1222–1242, <https://doi.org/10.1175/2010JPO4365.1>.
- Teixeira, M. A. C., 2014: The physics of orographic gravity wave drag. *Front. Phys.*, **2**, 43, <https://doi.org/10.3389/fphy.2014.00043>.
- Thomas, L. N., and J. R. Taylor, 2010: Reduction of the usable wind-work on the general circulation by forced symmetric instability. *Geophys. Res. Lett.*, **37**, L18606, <https://doi.org/10.1029/2010GL044680>.
- , —, R. Ferrari, and T. M. Joyce, 2013: Symmetric instability in the Gulf Stream. *Deep-Sea Res. II*, **91**, 96–110, <https://doi.org/10.1016/j.dsr2.2013.02.025>.
- , —, E. A. D'Asaro, C. M. Lee, J. M. Klymak, and A. Shcherbina, 2016: Symmetric instability, inertial oscillations, and turbulence at the Gulf Stream front. *J. Phys. Oceanogr.*, **46**, 197–217, <https://doi.org/10.1175/JPO-D-15-0008.1>.
- Umlauf, L., W. D. Smyth, and J. N. Moum, 2015: Energetics of bottom Ekman layers during buoyancy arrest. *J. Phys. Oceanogr.*, **45**, 3099–3117, <https://doi.org/10.1175/JPO-D-15-0041.1>.
- Vreugdenhil, C. A., and J. R. Taylor, 2018: Large-eddy simulations of stratified plane Couette flow using the anisotropic minimum-dissipation model. *Phys. Fluids*, **30**, 085104, <https://doi.org/10.1063/1.5037039>.
- Wang, P., J. Martin, and G. Morrison, 1999: Water quality and eutrophication in Tampa bay, Florida. *Estuarine Coastal Shelf Sci.*, **49** (1), 1–20, <https://doi.org/10.1006/ecss.1999.0490>.
- Warner, S. J., and P. MacCready, 2009: Dissecting the pressure field in tidal flow past a headland: When is form drag “real”? *J. Phys. Oceanogr.*, **39**, 2971–2984, <https://doi.org/10.1175/2009JPO4173.1>.
- , —, 2014: The dynamics of pressure and form drag on a sloping headland: Internal waves versus eddies. *J. Geophys. Res. Oceans*, **119**, 1554–1571, <https://doi.org/10.1002/2013JC009757>.
- Waterhouse, A. F., and Coauthors, 2014: Global patterns of diapycnal mixing from measurements of the turbulent dissipation rate. *J. Phys. Oceanogr.*, **44**, 1854–1872, <https://doi.org/10.1175/JPO-D-13-0104.1>.
- Wenegrat, J. O., and L. N. Thomas, 2020: Centrifugal and symmetric instability during Ekman adjustment of the bottom boundary layer. *J. Phys. Oceanogr.*, **50**, 1793–1812, <https://doi.org/10.1175/JPO-D-20-0027.1>.
- , J. Callies, and L. N. Thomas, 2018: Submesoscale baroclinic instability in the bottom boundary layer. *J. Phys. Oceanogr.*, **48**, 2571–2592, <https://doi.org/10.1175/JPO-D-17-0264.1>.
- Whitley, V., and J. Wenegrat, 2025: Breaking internal waves on sloping topography: Connecting parcel displacements to overturn size, interior-boundary exchanges, and mixing. *J. Phys. Oceanogr.*, **55**, 645–661, <https://doi.org/10.1175/JPO-D-24-0052.1>.
- Wienkers, A. F., L. N. Thomas, and J. R. Taylor, 2021: The influence of front strength on the development and equilibration of symmetric instability. Part 1. Growth and saturation. *J. Fluid Mech.*, **926**, A6, <https://doi.org/10.1017/jfm.2021.680>.
- Winters, K. B., P. N. Lombard, J. J. Riley, and E. A. D'Asaro, 1995: Available potential energy and mixing in density-stratified fluids. *J. Fluid Mech.*, **289**, 115–128, <https://doi.org/10.1017/S002211209500125X>.
- Zemskova, V. E., and N. Grisouard, 2021: Near-inertial dissipation due to stratified flow over abyssal topography. *J. Phys. Oceanogr.*, **51**, 2483–2504, <https://doi.org/10.1175/JPO-D-21-0007.1>.
- , —, 2022: Energetics and mixing of stratified, rotating flow over abyssal hills. *J. Phys. Oceanogr.*, **52**, 1155–1177, <https://doi.org/10.1175/JPO-D-21-0146.1>.